

Supporting Information

Implementing Vanadium Peroxides as Direct Air Carbon Capture Materials

Eduard Garrido Ribó,^{‡,a} Zhiwei Mao,^{‡,a} Jacob S. Hirschi,^a Taylor Lindsay,^a Karlie Bach,^a Eric D. Walter,^b Casey R. Simons,^c Tim J. Zuehlsdorff,^a May Nyman^{,a}*

^aDepartment of Chemistry, Oregon State University, Corvallis, OR 97331 United States.

^bPacific Northwest National Laboratory, Environmental Molecular Sciences Laboratory, Pacific Northwest National Laboratory, Richland, WA 99352

^cCAMCOR, University of Oregon, Eugene, OR 97331 United States.

Department of Chemistry, Oregon State University, OR 97330, United States

Table of Contents

Materials and Instrumentation	3
Elemental Analysis	3
FT-IR Spectroscopy	3
UV-vis Spectroscopy	3
Single Crystal X-Ray Diffraction	3
Thermogravimetric Analysis – Mass Spectroscopy (TGA-MS)	3
Computational Details	3
Solid-State	3
Cluster-Model	4
Synthetic Procedure for Tetraperoxovanadates	5
Potassium Tetraperoxovanadate, $K_3V(O_2)_4$	5
Rubidium Tetraperoxovanadate, $Rb_3V(O_2)_4$	5
Cesium Tetraperoxovanadate, $Cs_3V(O_2)_4$	5
Potassium oxodiperoxocarbonate, $K_3VO(O_2)_2CO_3$	6
NBT Tests	6
Alkali hydroxide tests	6
Tetraperoxovanadates tests	6
KO₂ Calibration Curve	6
EPR Measurements	6
Crystallographic data	8
Crystallographic Images	9
Bulk Characterization of compounds $K_3V(O_2)_4$, $Rb_3V(O_2)_4$, $Cs_3V(O_2)_4$	11

PXRD following the CO₂ capture process	12
Color change	13
FT-IR Spectra	14
Solid State NMR	16
Computational mechanisms	17
K₃VO₅CO₃ and KVO₃/KHCO₃ reference data	20
TGA-MS data and Curves	22
CHN Analysis	31
Superoxide Characterization	36
NBT Tests	36
EPR Characterization	40
Exploring superoxide through computation.	42
Carbon Capture technologies overview	44
References	49

Materials and Instrumentation

Elemental Analysis

The content of carbon was characterized using NC2500 ThermoQuest Elemental Analyzer fitted with a Costech Zero Blank Autosampler and ECS 4010 CHNSO Analyzer fitted with at Costech Zero Blank Autosampler, which belong to the Ocean Ecology and Biogeochemistry Facilities in the Oregon State University. The contents of K, Rb, and V were determined using a Horiba inductivity-coupled plasma (ICP) spectroscopy.

FT-IR Spectroscopy

The FT-IR spectra were collected using PerkinElmer Spectrum Two spectrometer in the range of 500 - 4000 cm^{-1} . Wavenumbers are given in cm^{-1} and intensities are demonstrated as s = strong, m = medium, w = weak, vs= very strong, br = broad, sh = sharp.

UV-vis Spectroscopy

The UV-vis absorbance spectra were obtained using a PerkinElmer Lambda 1050+ UV-Vis/NIR Spectrometer.

Single Crystal X-Ray Diffraction

Single-crystal X-ray diffraction for all structures were collected at 150 K, on a Rigaku Oxford Diffraction Synergy-S equipped with a PhototJet-S Cu source ($\lambda = 1.54178 \text{ \AA}$) and a HyPix-6000HE photon counting detector. All images were collected and processed using CrysAlisPro Versions 40.21a, 40.53, and 40.81a (Rigaku Oxford Diffraction, 2018). Data collection, data reduction, cell refinement, and experimental absorption correction were performed with the Bruker Apex2 software package. All calculations were performed using the SHELX program package with Olex2.

Thermogravimetric Analysis – Mass Spectroscopy (TGA-MS)

Thermogravimetric analysis (TGA) was performed on TA Instruments SDT Q600 and Mass Spectrometry (MS) was collected by Hiden Gas Analyzer HPR-20 QIC EGA. About 10 mg of the sample was transferred into alumina crucibles for measurements under Argon gas flow (the purge flow is 100 ml/min) up to 900 °C at the heating rate of 10 °C per minute.

Computational Details

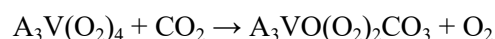
Solid-State

For the solid-state simulations, DFT^{1,2} unit-cell optimizations were carried out in CASTEP 20.11³ with the GGA functional PBE⁴ and BFGS⁵ algorithm. A 850 eV kinetic energy cutoff and 2x2x2 k-grid⁶ were

demonstrated to be adequate with CASTEP's on-the-fly generated norm-conserving pseudopotentials in convergence tests on $K_3VO(O_2)_2CO_3$. Phonon calculations at the gamma point were performed with the optimized structures through the density-functional perturbation theory (DFPT) method.⁷

Experimental crystal structures of $K_3V(O_2)_4$ and $K_3VO(O_2)_2CO_3$ were taken as starting geometries for the optimizations. The lowest energy structures from the Materials Project⁸ were taken for the remaining solid compounds. Vectors corresponding to the atomic displacements associated with the normal modes of vibration were made using jmol.⁹

Thermodynamic changes presented in the manuscript as solid-state were generated exclusively using CASTEP, except for the free energy thermal corrections for O_2 and CO_2 , which were taken from gas-phase calculations in Gaussian (details provided below). The reaction free energies for



(where A = K, Rb, or Cs) were calculated assuming idealized K-based structures, i.e. not using the experimentally based unit cells for Rb or Cs. The relative crystal stability of the vanadate reactants in said reaction were calculated based on the following scheme:

$$E_{rel. stab.} = E_{A_3V(O_2)_4} - 3E_{A^+}$$

where each energy value represents an electronic self-consistent field energy. The E_{A^+} value was obtained by placing the positively charged alkali ion in a periodic box of 35 x 35 x 35 Angstroms. An analogous approach was also used for the products.

Cluster-Model

To model the reaction mechanism, gas phase DFT geometry optimizations were performed in Gaussian 16 Rev. A.03¹⁰ with the range-separated hybrid functional CAM-B3LYP¹¹ with a 6-31+G* basis set for all atoms except the alkali counterions and Nb/Ta metal centers which were modeled with the LanL2DZ¹² effective core potential generated from the gaussian library. All minima and transition states were verified to have exclusively real frequencies and one imaginary frequency, respectively.

Inaccuracies of computed vibrational frequencies is likely an issue with the physical model/structure used for the calculation, and not a limitation of the computational method. From previous benchmarking studies, a typical error of 40 cm^{-1} can be expected for DFT vibrational energies with CAM-B3LYP/6-31+G*/LANL2DZ.¹³ Our computed frequencies are up to 92 cm^{-1} off from experiment, and could be due to the lack of inclusion of solvent effects from embedded water or hydrogen peroxide in these simulated

crystal structures. Despite this discrepancy, these energies are still broadly consistent with carbonate C=O vibrations, see for example figure 5 in reference.¹⁴

All structures are provided on this GitHub repository: https://github.com/tjz21/DAC_peroxovanadates

Synthetic Procedure for Tetraperoxovanadates

Potassium Tetraperoxovanadate, $\text{K}_3\text{V}(\text{O}_2)_4$

V_2O_5 (0.181 g, 1.0 mmol) was dissolved in 4M KOH (2.5 ml, 10.0 mmol), and then 30wt% H_2O_2 (2.05 ml, 20.1 mmol) was added to the mixture with stirring under the ice bath (0 – 5 °C). The solution turned clear purple and was then transferred to a 100 ml beaker with excess precooled ethanol (about 25 ml). Maintaining the stirring for approximately 15 minutes, the purple $\text{K}_3\text{V}(\text{O}_2)_4$ precipitated. After that, stirring was stopped, most of the ethanol was removed, and the slurry was refilled with methanol while in the ice bath. The final product was separated by vacuum filtration and washed with cold methanol to remove the impurities. **Yield:** 0.511 g (86.7 %, based on V).

Suitable single crystals were obtained by mixing the clear purple solution with cold ethanol in a 20 ml scintillation vial and maintained at 0 °C without stirring. Deep purple crystals appeared overnight.

Rubidium Tetraperoxovanadate, $\text{Rb}_3\text{V}(\text{O}_2)_4$

V_2O_5 (0.181 g, 1.0 mmol) was dissolved in 4M RbOH (2.5 ml, 10.0 mmol), and then 30wt% H_2O_2 (2.05 ml, 20.1 mmol) was added to the mixture with stirring under the ice bath (0 – 5 °C). The solution turned purple with some unreacted V_2O_5 at the bottom. Only the upper clear purple solution was transferred to a 100 ml beaker with excess precooled ethanol (about 25 ml). Maintaining the stirring for approximately 20 minutes, the purple $\text{Rb}_3\text{V}(\text{O}_2)_4$ precipitated. After that, stirring was stopped, most of the ethanol was removed, and the slurry was refilled with methanol while in the ice bath. The final product was separated by vacuum filtration and washed with cold methanol to remove the impurities. **Yield:** 0.836 g (96.5 %, based on V).

Suitable single crystals were obtained by transferring a small portion of the upper clear purple solution into a 5 ml vial which was stored in sealed a 20 ml scintillation vial containing ethanol. Slow vapor diffusion in the refrigerator at 5°C produced deep purple crystals of compound **2** overnight.

Cesium Tetraperoxovanadate, $\text{Cs}_3\text{V}(\text{O}_2)_4$

Compound **3** was synthesized by following the same procedure as compound **1** with the difference of using 4M CsOH (2.5 ml, 10.0 mmol) instead of 4M KOH. **Yield:** 0.947 g (82.3 %, based on V). Since the Cs-analogue is more reactive, the operations were performed as quickly as possible.

Suitable single crystals were obtained by transferring a small portion of the upper clear purple solution into a 5 ml vial which was stored in sealed a 20 ml scintillation vial containing ethanol. Before sealing both vials, Ar gas was used to flush the solution in the small vial and the ethanol in the large vial for 5 minutes. Slow vapor diffusion in the refrigerator at 5°C produced deep purple crystals overnight.

Potassium oxodiperoxocarbonate, $K_3VO(O_2)_2CO_3$

Synthesis of $K_3VO(O_2)_2CO_3$ was adapted from literature.¹⁵ Briefly, V_2O_5 (0.23 g, 1.2 mmol) and K_2CO_3 (10 g, 72.4 mmol) were suspended in 1.5 wt% H_2O_2 (50ml, 22 mmol) with stirring. Once the solids were dissolved, the sample was placed in an open beaker and kept at 5 °C undisturbed. Yellow crystals appeared within one week.

NBT Tests

Alkali hydroxide tests.

These tests were adapted from previous work performed on aqueous mixtures of sodium hydroxide, hydrogen peroxide and NBT.¹⁶ 1.25 mL of a 0.05 M solution of KOH was mixed with 4 mL of a 0.6 mM solution of NBT. Then, 29 μ L of 15 % H_2O_2 were added, causing a colour change from pale yellow to purple. This solution was monitored over time as the solution darkened progressively. After long periods of time standing, the insoluble NBT-formazan product precipitates.

Tetraperoxovanadates tests

5.25 mL of 0.46 mM NBT solution were added to 0.065 mmol of tetraperoxovanadate (18.7 mg for the K-analogue, 32.5 mg for the Rb-analogue and 39.5 mg for the Cs-analogue). These masses were used for both fresh and decomposed tests. The solid dissolved rapidly and the solution was monitored over time, starting when the purple colour of vanadium-bound peroxide disappeared. Both linear and power law fits of the curves were attempted, in order to extrapolate the data to time=0. These are summarized in **Table S10**.

KO₂ Calibration Curve

A stock solution was prepared by adding 50 mL of 0.7 mM NBT solution into a glass vial containing 5.2 mg of KO_2 , giving a final concentration of 1.46 mM of KO_2 . The solid dissolved quickly and produced a purple solution. A set of standards were created by diluting the stock solution to the following concentrations: 0.91 mM, 0.73 mM, 0.55 mM, 0.37 mM and 0.29 mM.

EPR Measurements

EPR spectra were recorded with a Bruker ELEXSYS E580 spectrometer equipped with a SHQE resonator. The typical settings for the spectra were microwave frequency = 9.32 GHz, sweep width = 3000 G, sweep time = 82 s, power = 20.0 mW, field modulation amplitude = 5.0 G. Samples were contained in 4mm OD FEP tubes (Wilmad). Temperature-dependent spectra were acquired using a Bruker continuous flow nitrogen cryostat and BVT 3000 controller.

To quantify the superoxide in the peroxovanadates, we also performed an EPR measurement on a 1000 ppm standard solution of copper imidazolate, and the area under the curve translates to number of spins as a reference for the superoxide signals from the peroxovanadate compounds (predetermined weights). From the formula weights of these compounds, based on both crystal structure and TGA weight loss data, we determined the mole percent of superoxide present; assuming the following charge-balance replacement:



These results are summarized in **Table S11**.

Crystallographic data

Table S1. Crystallographic data

Compound	2	3
CCDC	2264013	2264012
Formula	O ₁₃ Rb ₃ V	Cs ₃ O ₁₁ V
Crystal system	Monoclinic	Monoclinic
Temperature (K)	229.99(10)	149.99(10)
Space group	P2 ₁ /n	P2 ₁ /n
a (Å)	6.8447(2)	8.4013(3)
b(Å)	23.2894(5)	12.0178(4)
c (Å)	7.8276(2)	11.5178(5)
β°	112.399(3)	91.359(4)
Volume (Å ³)	1153.65(6)	1162.57(8)
Z	4	4
Density (calculated) (g/cm ³)	2.967	3.575
Absorption coefficient (mm ⁻¹)	23.179	10.149
Radiation	Cu Kα (λ = 1.54184)	Mo Kα (λ = 0.71073)
Index ranges	-8 ≤ h ≤ 8, -29 ≤ k ≤ 29, -9 ≤ l ≤ 9	-11 ≤ h ≤ 12, -17 ≤ k ≤ 13, -13 ≤ l ≤ 16
Reflections collected	12272	11316
Independent reflections	2365 [Rint = 0.0969, Rsigma = 0.0502]	3429 [Rint = 0.0503, Rsigma = 0.0447]
Goodness-of-fit on F2	1.117	1.018
Final R indices [I>2σ(I)]	R1 = 0.0583, wR2 = 0.1638	R1 = 0.0320, wR2 = 0.0816
R indices (all data)	R1 = 0.0583, wR2 = 0.1638	R1 = 0.0419, wR2 = 0.0853
Largest diff. peak/hole (e Å ⁻³)	1.54/-0.88	1.92/-1.29

Crystallographic Images

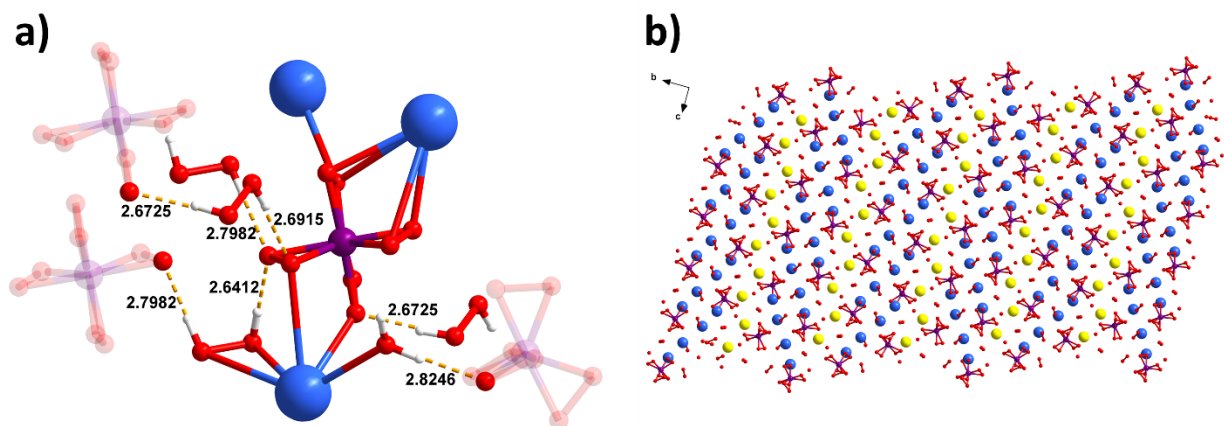


Figure S1. a) Ball and stick representation of compound **2** and its surrounding environment. The distances between the solvent molecules and the different peroxide ligands bound to the central vanadium atom are marked as discontinuous orange bonds. Their average distance of 2.7 Å indicates H-bonding, further confirming the fact that the free peroxide ligands are indeed protonated. In this depiction, hydrogen atoms were included for clarity, however, these were not found by x-ray diffraction. b) Extended crystal packing of compound **2** seen from the *a*-axis. It can be seen how the Rb cations arrange in a zigzag pattern along the *bc* plane, with Rb1 and Rb3 arranged in series of 4 and Rb2 creating a node in between. Rb2 are colored yellow for clarity. V: violet. Rb: dark blue. O: red. H: white

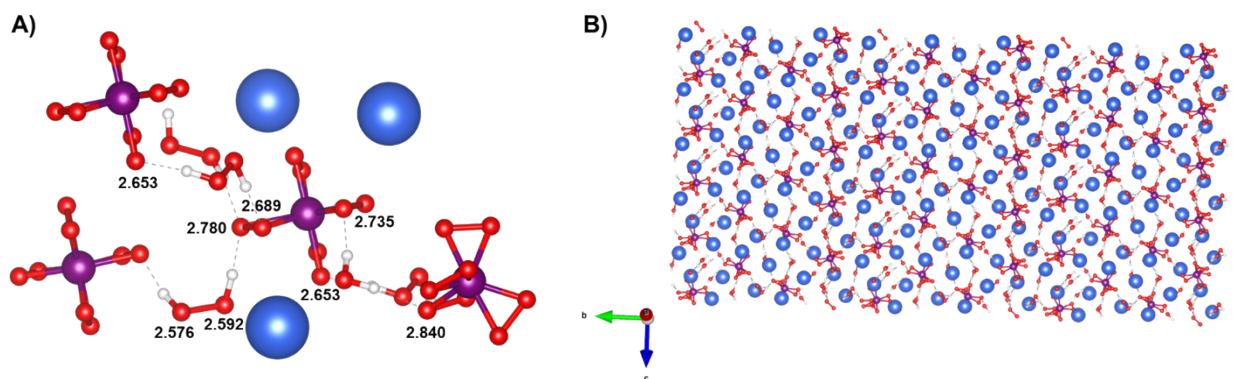


Figure S2. Segment of the computationally predicted unit cell for $\text{Rb}_3\text{V}(\text{O}_2)_4(\text{H}_2\text{O})_1(\text{H}_2\text{O}_2)_2$ with selected O-O distances displayed in angstroms. This structure was generated by explicitly adding hydrogens to the experimental crystal geometry, which was then optimized using DFT. (b) A supercell arrangement of the same structure viewed along the *c*-axis.

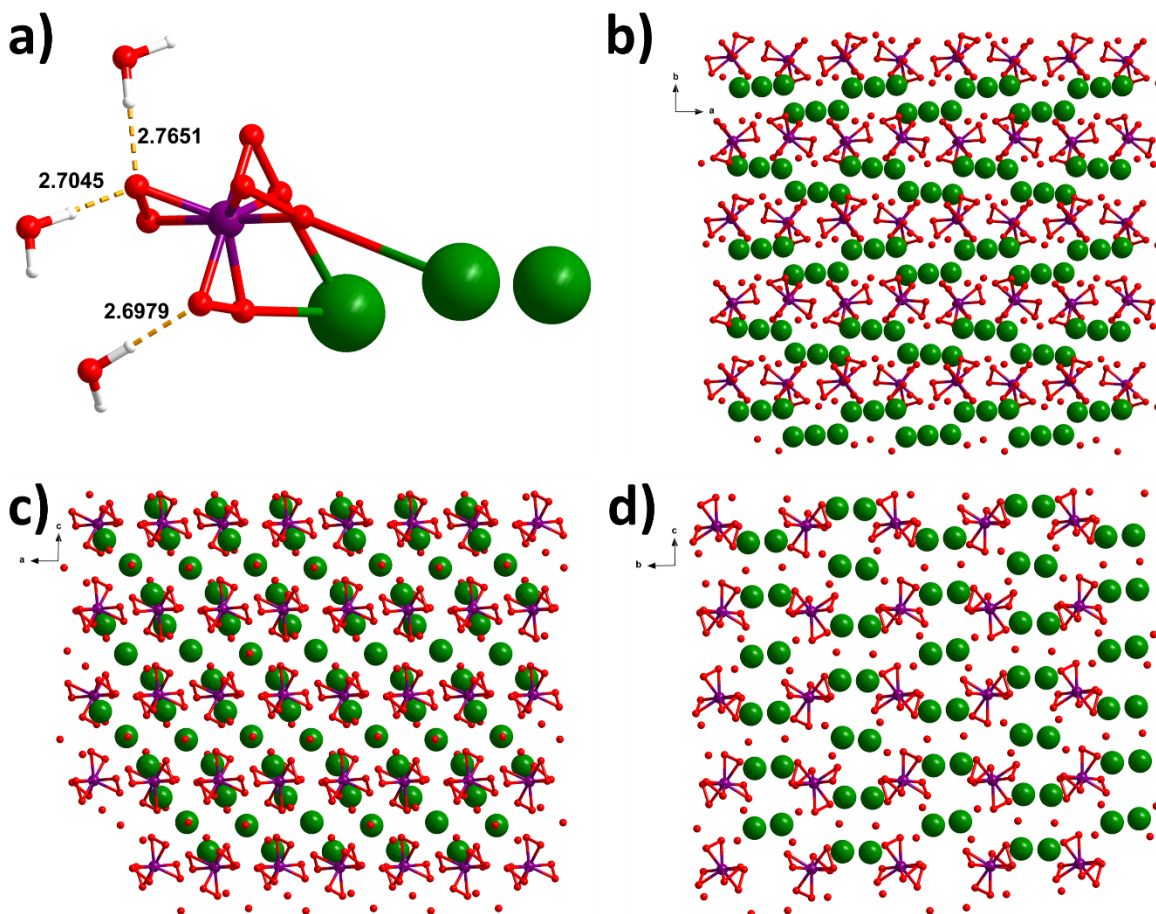


Figure S3. a) Ball and stick representation of compound **3** and its surrounding environment. The distances between the solvent molecules and the different peroxide ligands bound to the central vanadium atom are marked as discontinuous orange bonds. Their average distance of 2.7 Å indicates H-bonding. In this depiction, hydrogen atoms were included for clarity, however, these were not found by x-ray diffraction. b) Extended crystal packing of compound **3** seen from the c-axis. c) Extended crystal packing of compound **3** seen from the b-axis. d) Extended crystal packing of compound **3** seen from the a-axis. V: violet. Cs: green. O: red.

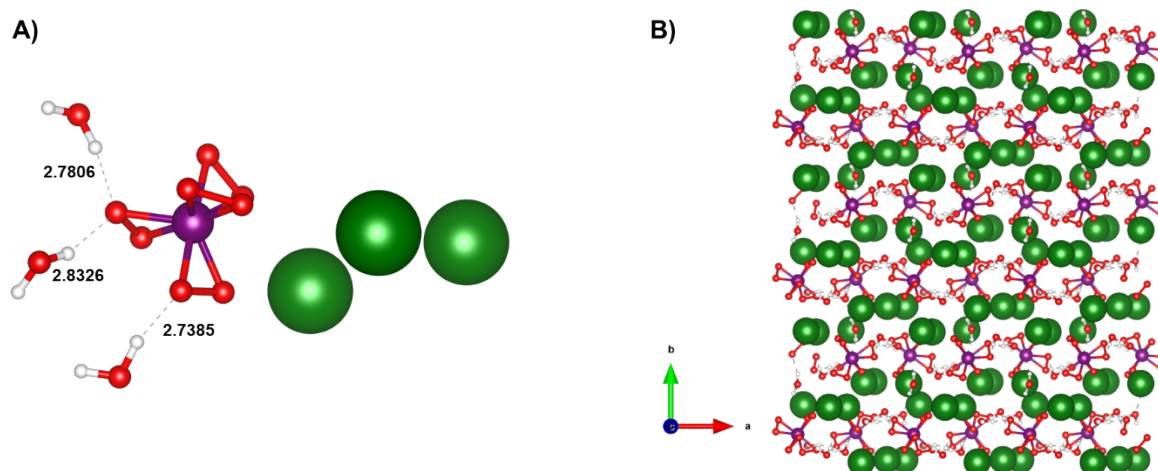


Figure S4. Segment of the DFT-optimized unit cell of $\text{Cs}_3\text{V}(\text{O}_2)_4(\text{H}_2\text{O})_3$ with selected O-O distances displayed in angstroms. (b) The same structure viewed along the c-axis.

Bulk Characterization of compounds $\text{K}_3\text{V}(\text{O}_2)_4$, $\text{Rb}_3\text{V}(\text{O}_2)_4$, $\text{Cs}_3\text{V}(\text{O}_2)_4$

Table S2. Summary of TGA results

Compound	TGA weight loss (experimental)	Theoretical weight loss assuming no extra-framework molecules ¹	Maximum wt % extraframework molecules
1 (K analogue)	22.0%	21.6%	N/A
2 (Rb analogue)	16.6%	14.7%	~2% ²
3 (Cs analogue)	11.3%	11.1%	N/A

¹calculated by the reaction $\text{A}_3\text{VO}_8 \rightarrow \Delta \rightarrow \text{A}_3\text{VO}_4 + 2\text{O}_2$

² ~2% mass is the equivalent of 8.9 mass units, or approximately half a water molecule or a fourth of a peroxide molecule

PXRD following the CO₂ capture process

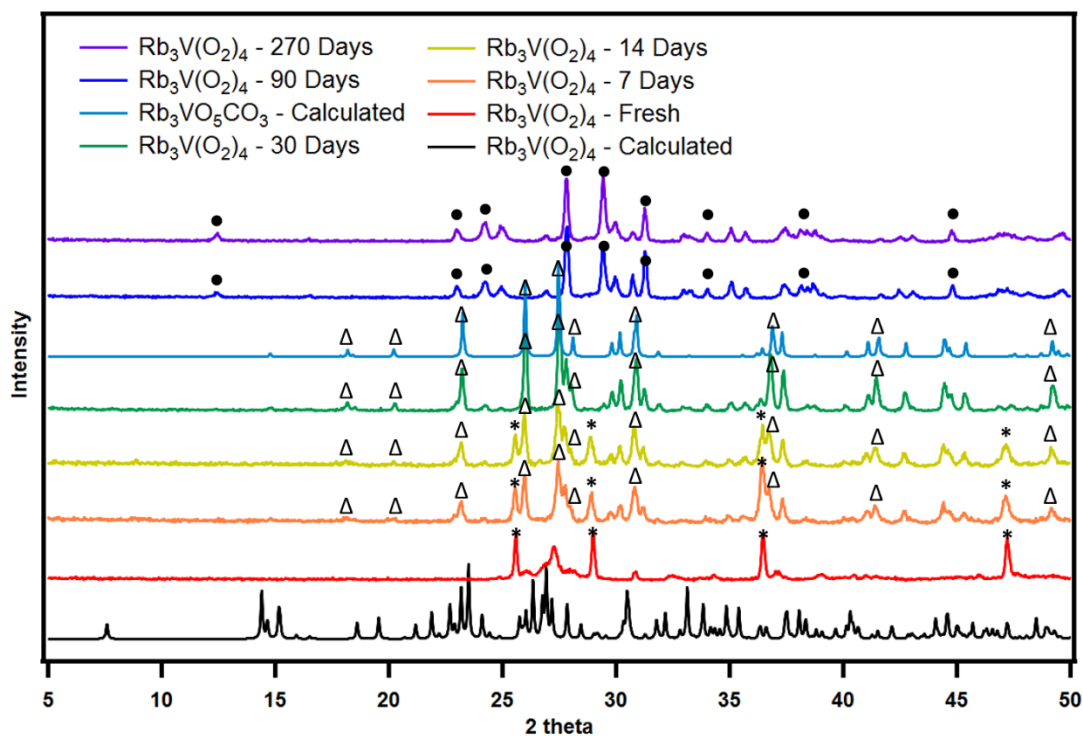


Figure S5. PXRD patterns for $\text{Rb}_3\text{V}(\text{O}_2)_4$ being exposed to the air over time. After 30 days exposure to the air, new peaks (marked with Δ) indicate the formation of $\text{Rb}_3[\text{VO}(\text{O}_2)_2(\text{CO}_3)]$, and the result matched with the calculation of $\text{Rb}_3[\text{VO}(\text{O}_2)_2(\text{CO}_3)]$ single crystal result. When the sample was left over 90 days, extra peaks (marked with •) suggest the structure has changed while the old structure was completely decomposed.

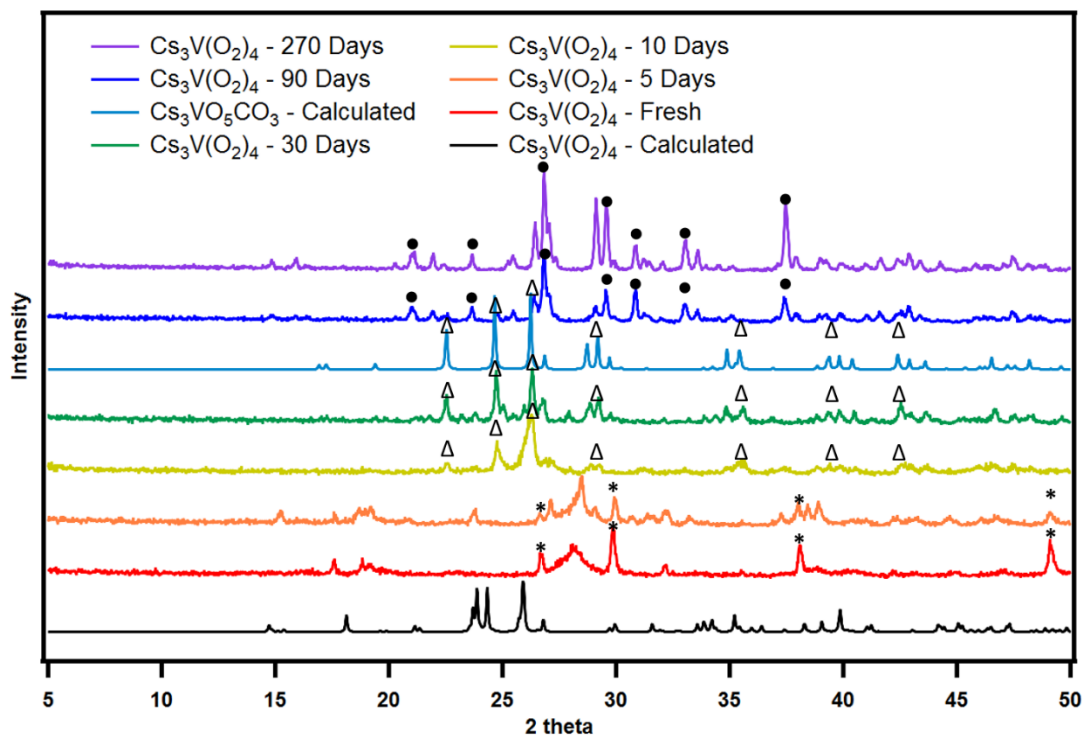


Figure S6. PXRD patterns for $\text{Cs}_3\text{V}(\text{O}_2)_4$ being exposed to the air over time. After 30 days exposure to the air, new peaks (marked with Δ) indicate the formation of $\text{Cs}_3[\text{VO}(\text{O}_2)_2(\text{CO}_3)]$, and the result matched with the calculation of $\text{Cs}_3[\text{VO}(\text{O}_2)_2(\text{CO}_3)]$ single crystal result. When the sample was left over 90 days, extra peaks (marked with \bullet) suggest the structure has changed while the old structure was completely decomposed.

Color change

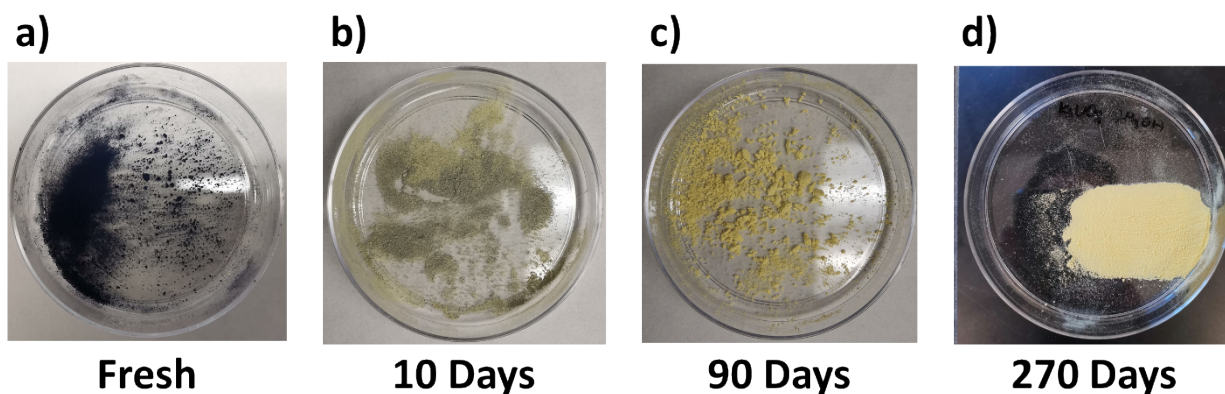


Figure S7. Gradual colour change of $\text{K}_3\text{V}(\text{O}_2)_4$ upon extended exposure to ambient conditions.

FT-IR Spectra

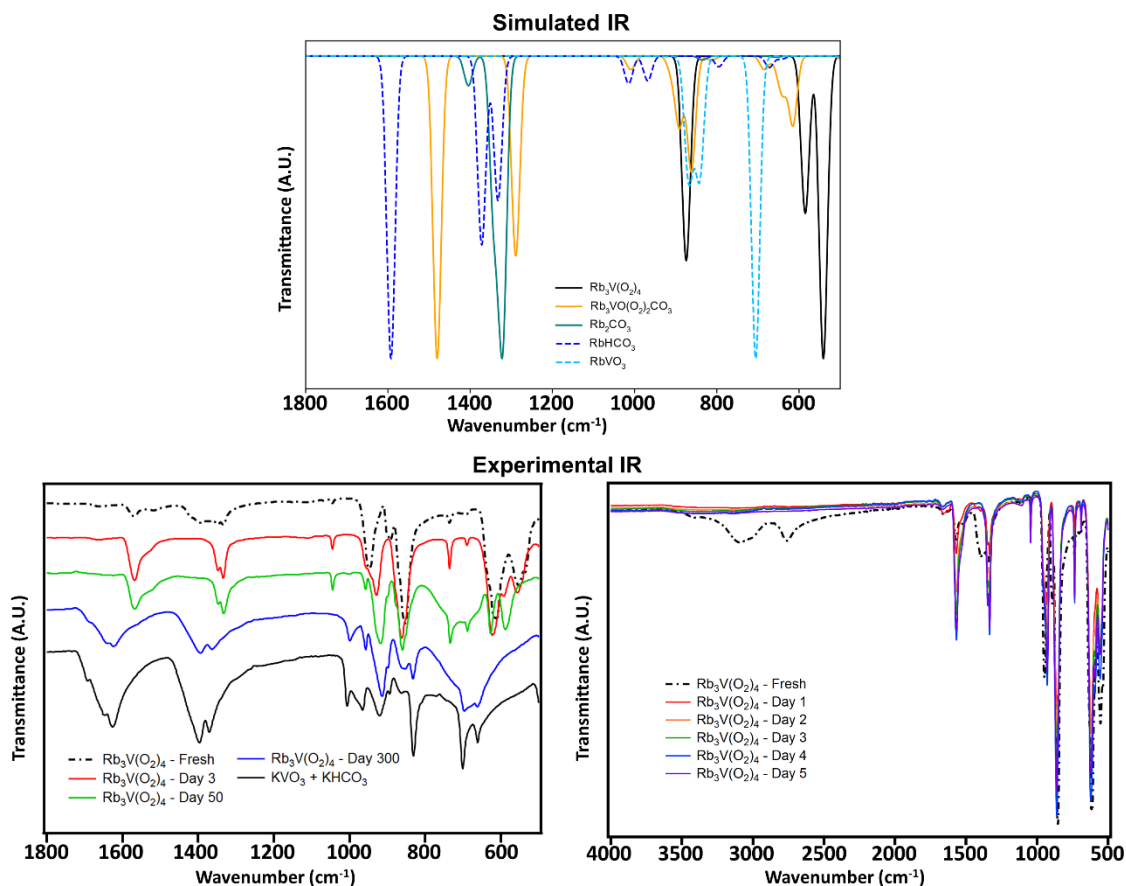


Figure S8. FTIR spectra of $\text{Rb}_3\text{V}(\text{O}_2)_4$ capturing CO_2 over time in the spectral range between 1800 and 500 cm^{-1} with comparison to KHCO_3 , and KVO_3 (Bottom left). Full spectrum is included (bottom right) showing no peaks beyond 2000 cm^{-1} . Representative carbonate peaks for $\text{Rb}_3[\text{VO}(\text{O}_2)_2(\text{CO}_3)]$ (1570 cm^{-1} , 1335 cm^{-1} , and 1045 cm^{-1}) are observed in Day 3 and Day 30 samples. The spectrum of Day 300 one matches the IR results of KHCO_3 (1630 cm^{-1} , 1390 cm^{-1} , and 1010 cm^{-1}) and KVO_3 (965 cm^{-1} , and 890 cm^{-1}).

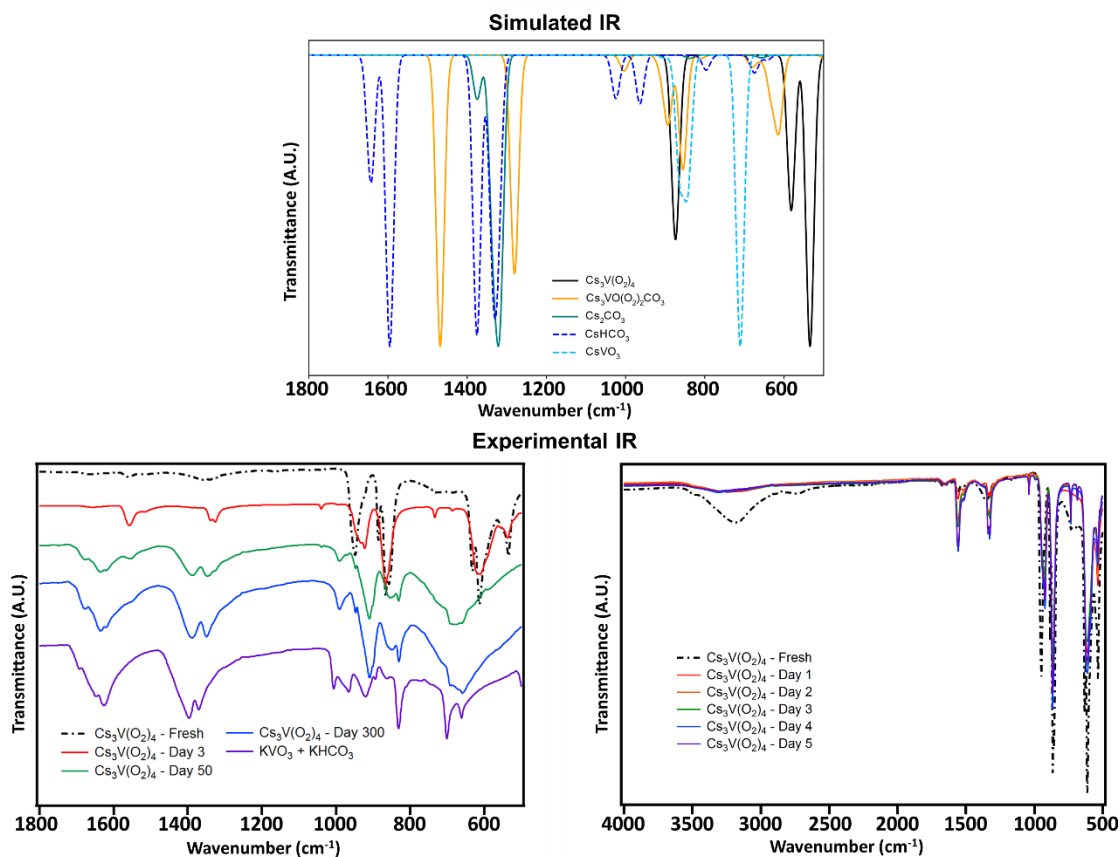


Figure S9. FTIR spectra of $\text{Cs}_3\text{V}(\text{O}_2)_4$ capturing CO_2 over time in the spectral range between 1800 and 500 cm^{-1} with comparison to KHCO_3 , and KVO_3 (Bottom left). Full spectrum is included (bottom right) showing no peaks beyond 2000 cm^{-1} . Representative carbonate peaks for $\text{Cs}_3[\text{VO}(\text{O}_2)_2(\text{CO}_3)]$ (1560 cm^{-1} , 1330 cm^{-1} , and 1040 cm^{-1}) are observed in Day 3 and Day 30 samples. The spectrum of Day 300 one matches the IR results of KHCO_3 (1630 cm^{-1} , 1390 cm^{-1} , and 1010 cm^{-1}) and KVO_3 (965 cm^{-1} , and 890 cm^{-1}).

Table S3. Carbonate FTIR Peak Assignments for $\text{A}_3\text{V}(\text{O}_2)_4$ after capturing CO_2 under ambient conditions with the transition to $\text{A}_3[\text{VO}(\text{O}_2)_2(\text{CO}_3)]$.

Material ($\text{A}_3\text{V}(\text{O}_2)_4$)	Asymmetric Stretching (ν_3 , cm^{-1})		Asymmetric Stretching (ν_3' , cm^{-1})		Symmetric Stretching (ν_1 , cm^{-1})	
	Experimental	Computational	Experimental	Computational	Experimental	Computational
$\text{K}_3[\text{V}(\text{O}_2)_4]$	1570	1484	1340	1296	1050	1014
$\text{Rb}_3[\text{V}(\text{O}_2)_4]$	1570	1480	1335	1289	1045	1009
$\text{Cs}_3[\text{V}(\text{O}_2)_4]$	1560	1468	1330	1280	1040	1004

Solid State NMR

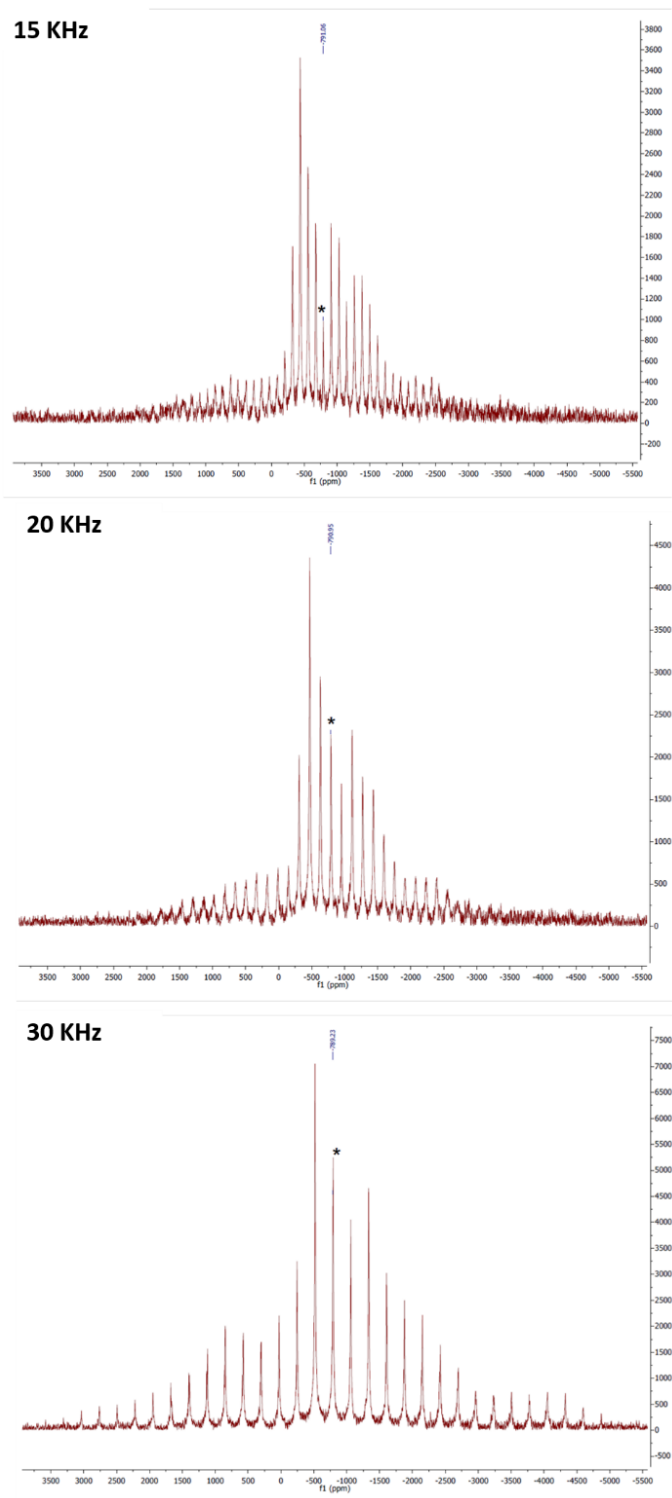


Figure S10. ^{51}V MAS NMR spectra of $\text{K}_3\text{V}(\text{O}_2)_4$. The central peak at 789 ppm was determined by changing the spin speeds.

Computational mechanisms

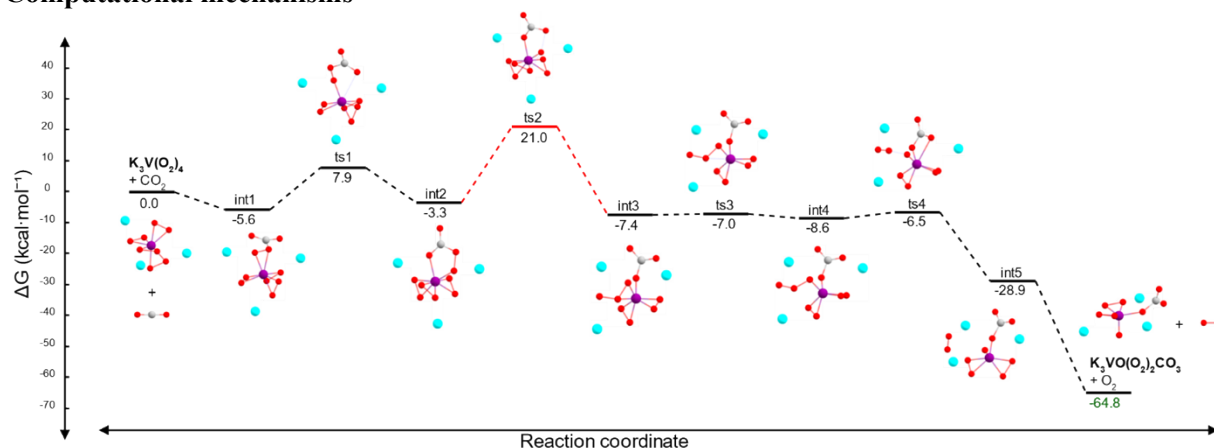


Figure S11. A series of five intermediates and four transition states that connect the reactant, $\text{K}_3\text{V}(\text{O}_2)_4$, to the CO_2 addition product, $\text{K}_3\text{VO}(\text{O}_2)_2\text{CO}_3$. Of the four steps— CO_4 isomerization, O atom transfer, O_3 rearrangement, and O-O cleavage—the $\text{int2} \rightarrow \text{int3}$ O atom transfer highlighted in red is predicted to be the rate-determining.

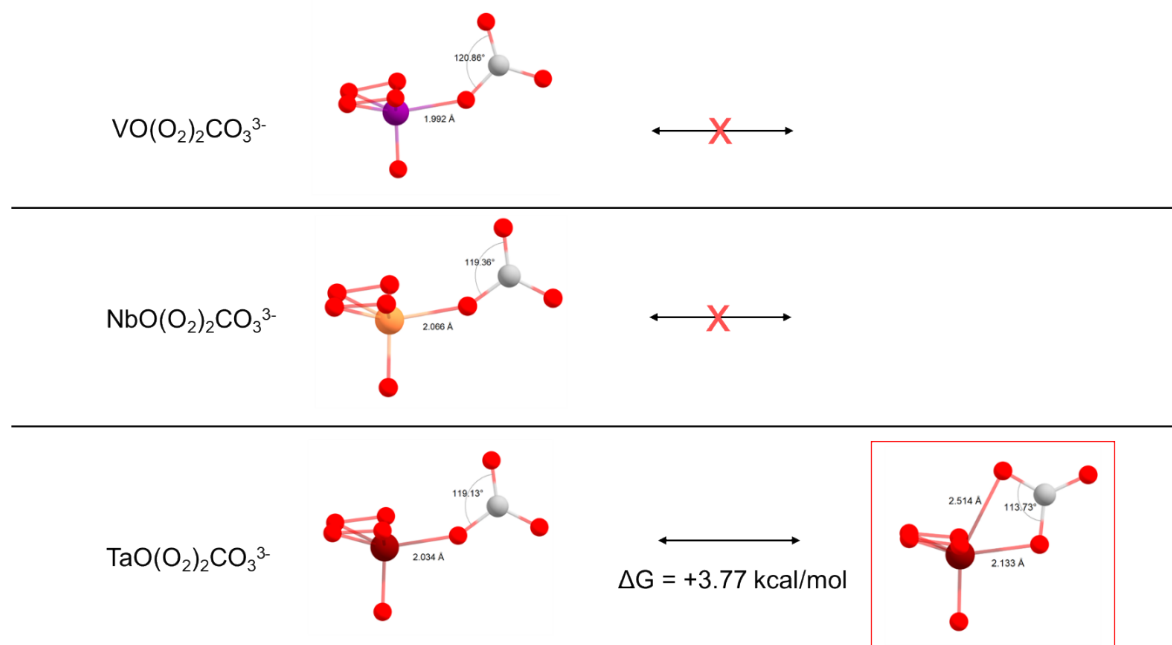


Figure S12. Cluster-model DFT calculations of the anionic complexes $[\text{VO}(\text{O}_2)_2\text{CO}_3]^{3-}$, $[\text{NbO}(\text{O}_2)_2\text{CO}_3]^{3-}$, and $[\text{TaO}(\text{O}_2)_2\text{CO}_3]^{3-}$. The bidentate CO_3 orientation only becomes kinetically stable with Ta.

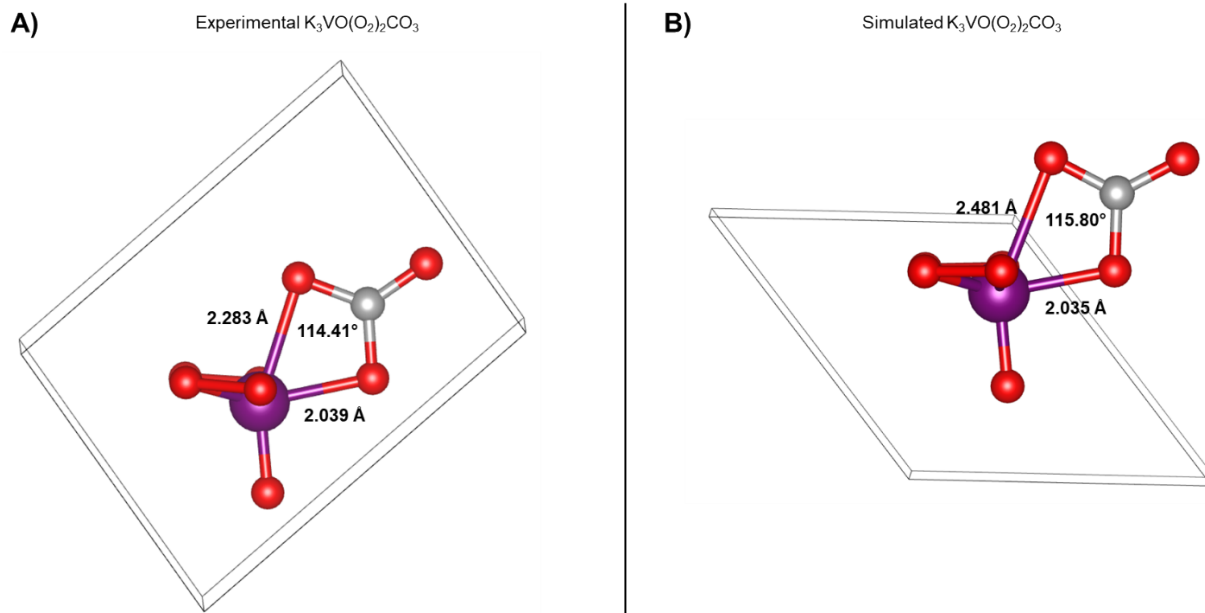


Figure S13. (A) Experimental crystal structure of $\text{K}_3\text{VO}(\text{O}_2)_2\text{CO}_3$ with the potassium counterions removed for clarity. (B) DFT-optimized structure with periodic boundary conditions presented in the same style, which features bidentate coordination of the CO_3 , albeit with highly asymmetric V-O bond lengths for the coordinating oxygen atoms: 2.481 vs 2.035 Å. This asymmetry is also observed, albeit to a lesser extent, in the experimental crystal structure. Therefore, the chemically suspicious monodentate geometry of CO_3 in the cluster-model $\text{K}_3\text{VO}(\text{O}_2)_2\text{CO}_3$ calculations is attributed to (1) the small atomic radius of the V^{5+} metal center and (2) the lack of crystal packing effects. The κ^1 - CO_3 geometry of the product is not expected to impact the $\text{int2} \rightarrow \text{int3}$ (Figure S49) rate-determining step of the mechanism.

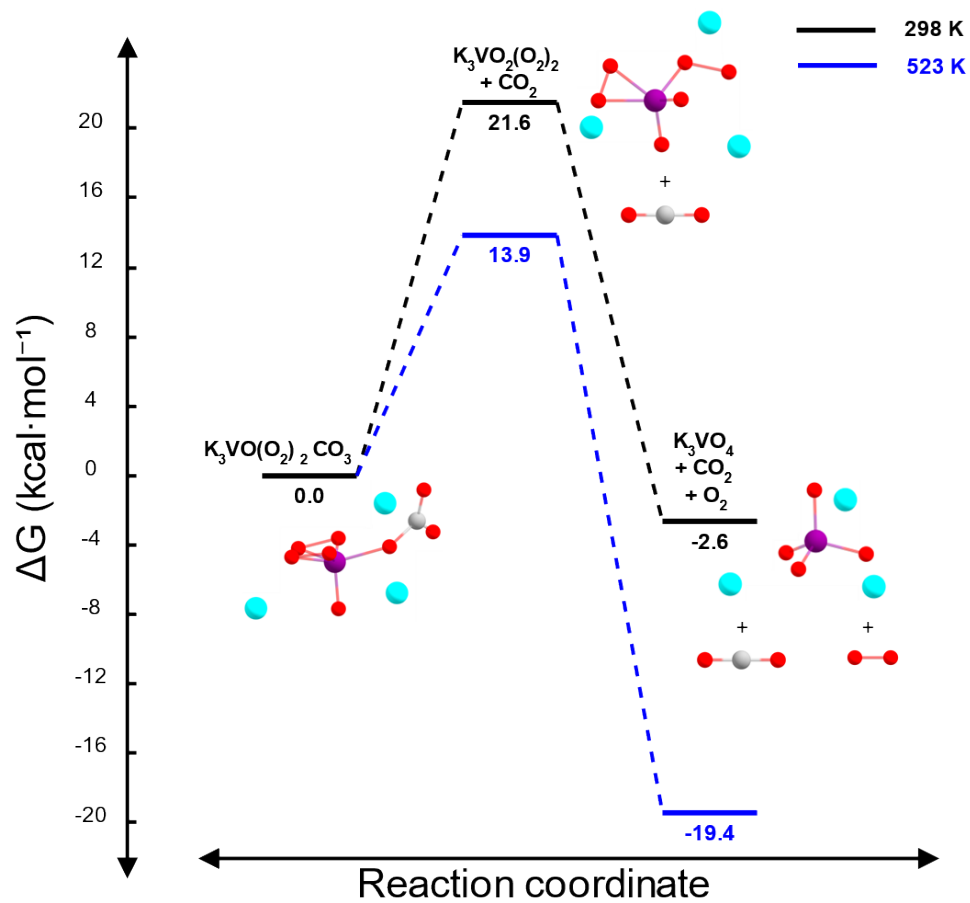


Figure S14. Two-step process for the decomposition of $\text{K}_3\text{VO}(\text{O}_2)_2\text{CO}_3$ into K_3VO_4 . The mechanism sequence is (1) uphill removal of CO_2 and (2) downhill removal of O_2 . The reaction is predicted to become more spontaneous at elevated temperatures.

$K_3VO_5CO_3$ and $KVO_3/KHCO_3$ reference data

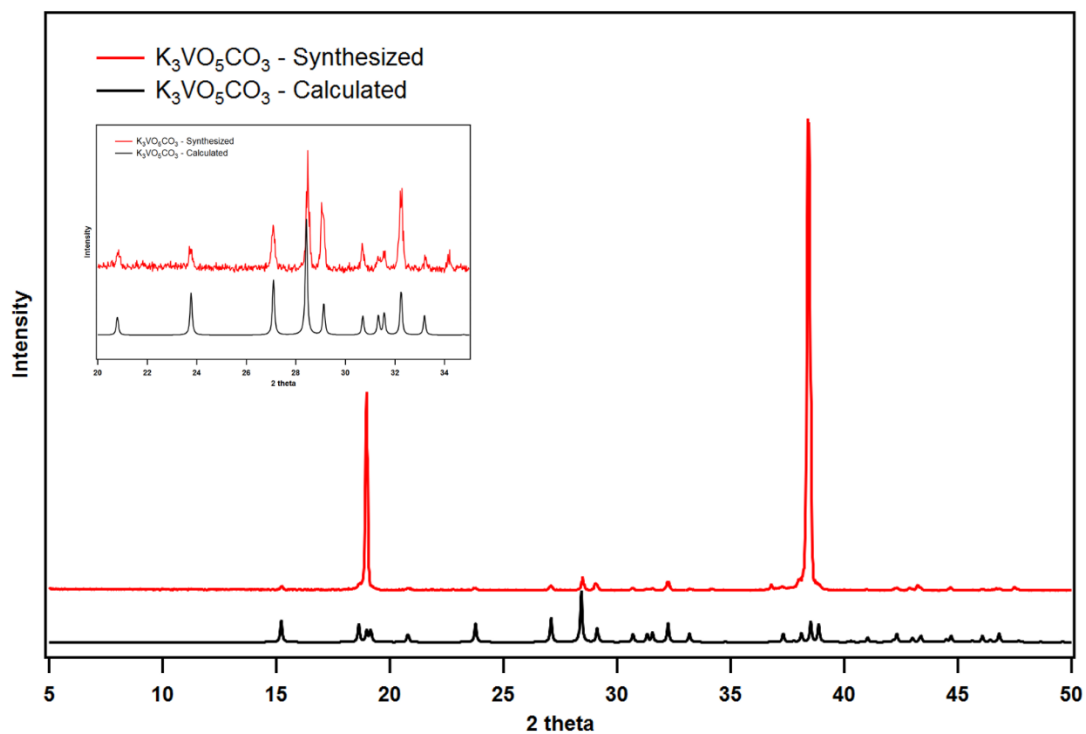


Figure S15. The PXRD illustration of synthesized $K_3VO_5CO_3$ pattern with the calculated result of its single crystal data and a zoomed view from 20° to 35° is shown in the picture.

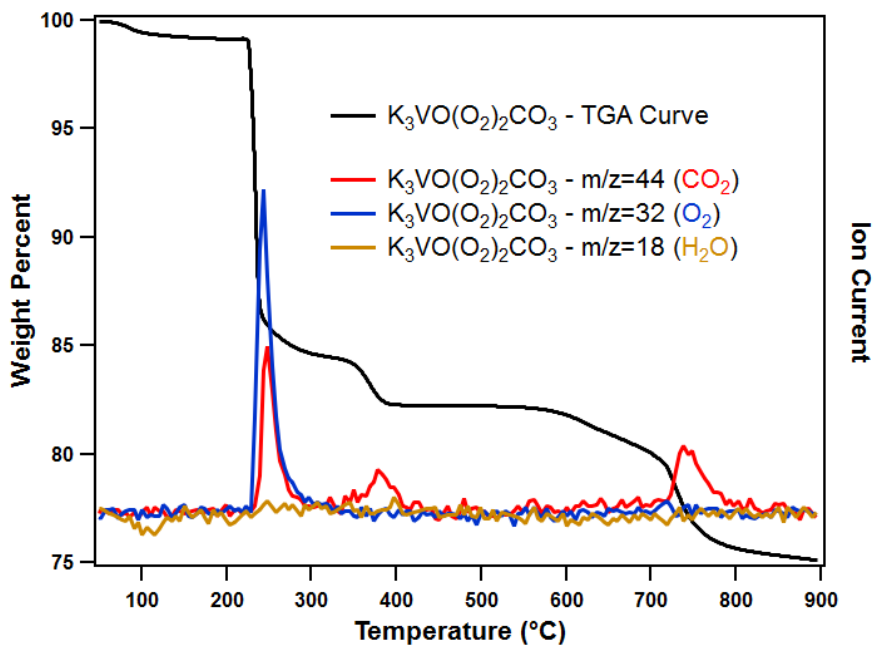


Figure S16. TGA-MS spectrum for synthesized $K_3[VO(O_2)_2CO_3]$. The CO_2 has a weight percent of 15.03 % (theoretical: 14.27 %); the O_2 is 9.31 % (theoretical: 10.38 %), and the water takes 0.56 %.

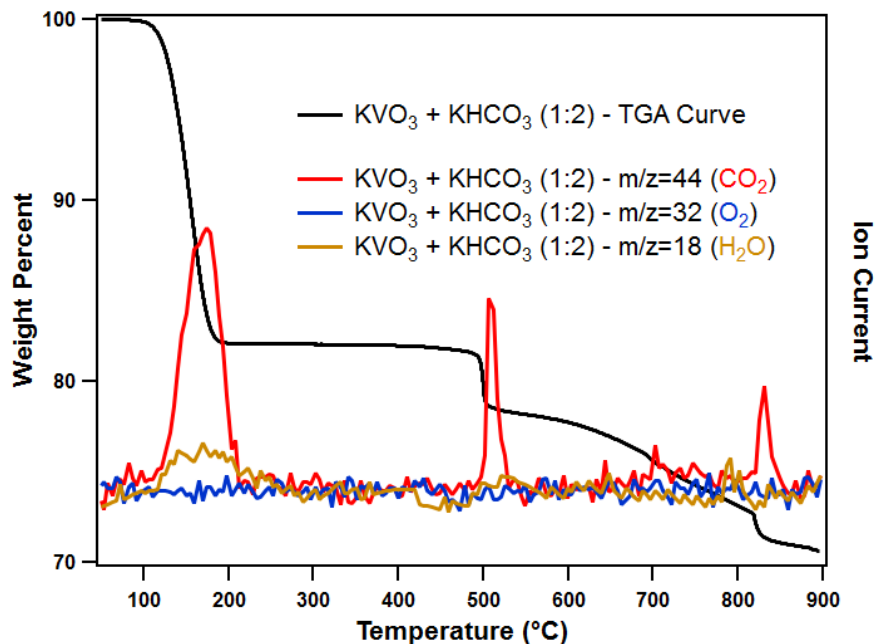


Figure S17. TGA-MS spectrum for mixed KVO_3 and KHCO_3 (moles ratio = 1:2). The KHCO_3 is decomposed around 180 °C with 17.94 % weight loss (theoretical: 19.00 %) corresponding to 1 unit H_2O and 1 unit CO_2 . After the conversion, with the existence of vanadate, residue carbonate can be catalyzed by vanadium source and release CO_2 around 500 °C. Then, carbonate bonded to potassium is further removed up to 900 °C (11.52% in total).

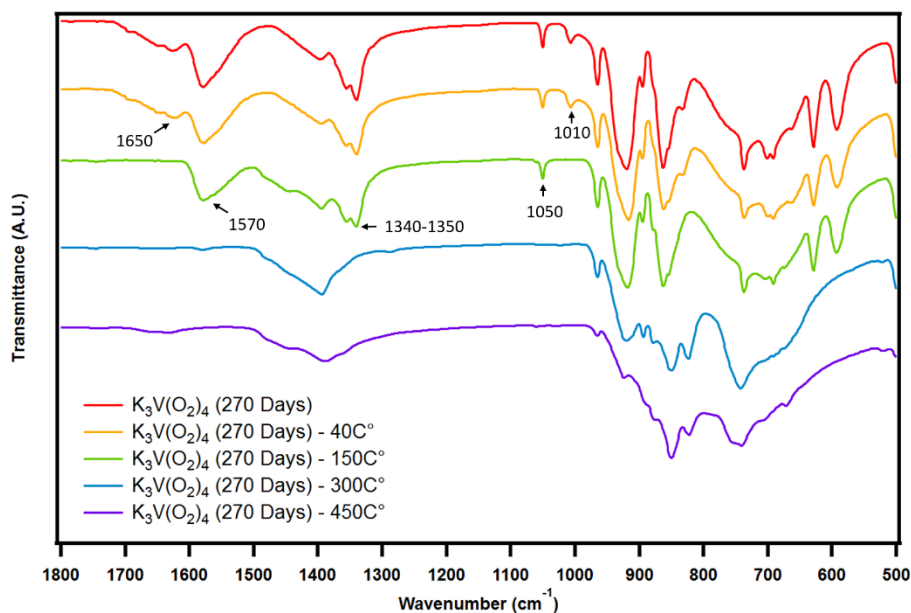


Figure S18. FTIR spectra for decomposed $K_3V(O_2)_4$ (being exposed to the air for 270 days) with isothermal treatments at 40 °C, 150 °C, 300 °C, and 450 °C for 30 minutes. Compared to the $K_3[VO(O_2)_2(CO_3)]$, extra peaks at 1650 cm^{-1} and 1010 cm^{-1} correspond to the bicarbonate structure and this compound is stable when the temperature is 40 °C. With increasing temperature, the disappearance of these mentioned peaks suggests the bicarbonate is removed from the material and the IR spectrum at 150 °C matches the compound of $K_3[VO(O_2)_2(CO_3)]$ (1570 cm^{-1} , 1350 cm^{-1} , and 1050 cm^{-1}). At higher temperatures, the product turns to a mixture of different vanadates.

TGA-MS data and Curves

Table S4. Results of TGA-MS weight percent loss assigned to different released gasses of $K_3V(O_2)_4$ after time study experiments under ambient conditions. The associated carbon weight percent content and molar ratio between C/V were also calculated.

Species	CO ₂ %	O ₂ %	H ₂ O %	C%	C:V Ratio
Fresh	-	18.6	2.42	-	-
Day 5	8.29	13.4	2.26	2.26	0.57
Day 10	10.4	13.5	2.16	2.83	0.72
Day 30	12.4	8.48	0.20	3.37	0.86
Day 90	17.7	3.56	4.01	4.84	1.25
Day 270	21.2	2.88	3.28	5.77	1.51

Table S5. Results of TGA-MS Data of $\text{Rb}_3\text{V}(\text{O}_2)_4$ Carbon Capture Time Study Experiments under Ambient Conditions.

Species	CO_2 %	O_2 %	H_2O %	C%	C:V Ratio
Fresh	1.45	13.5	1.52	-	-
Day 5	5.66	7.40	1.37	1.54	0.56
Day 10	7.20	5.30	1.77	1.96	0.71
Day 30	9.43	5.30	0.84	2.57	0.94
Day 90	17.5	-	3.54	4.76	1.86
Day 270	18.4	-	4.09	5.00	1.99

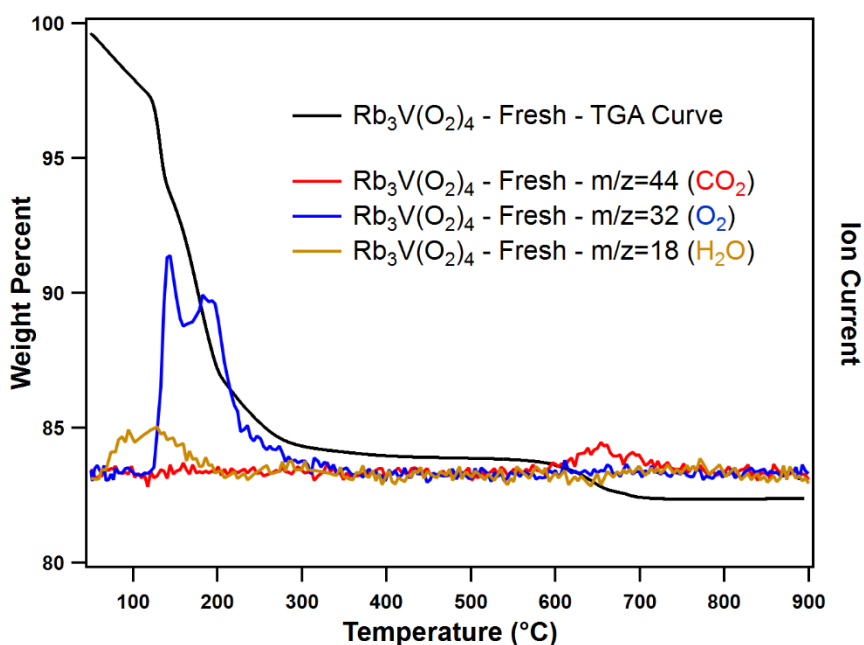


Figure S19. TGA curve and MS spectra for fresh synthesized $\text{Rb}_3\text{V}(\text{O}_2)_4$. The first weight loss in the temperature range of 60 °C to 105 °C is assigned to a small amount of water (experimental: 1.52 wt %). The continued weight loss from 105 °C to 300 °C originated from the four peroxide ligands bonded to the vanadium center (experimental: 13.46 wt %, theoretical: 14.70 wt %). Some carbon dioxide signals were detected around 600 °C to 750 °C due to the fresh compound 2 quickly reacting to CO_2 in the air.

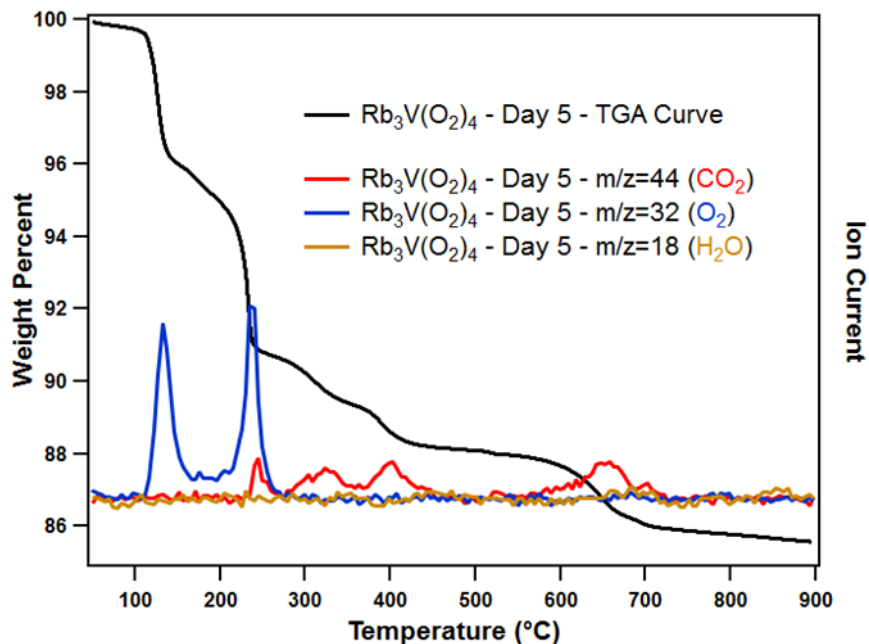


Figure S20. TGA curve and MS spectra for $\text{Rb}_3\text{V}(\text{O}_2)_4$ after being exposed to ambient conditions for 5 days. The TGA-MS shows a stepwise thermal decomposition process associated with (i) molecular oxygen from unreacted peroxide ligands bound to the vanadium metal center (100 – 195 °C), (ii) oxygen and carbon dioxide from peroxides and carbonates bonded to vanadium (195 – 280 °C), and (iii) carbon dioxide from carbonates bonded to alkali metals (280 – 900 °C). The CO_2 has a weight percent of 5.66 %; the O_2 is 7.40 %, and the water takes 1.37 %.

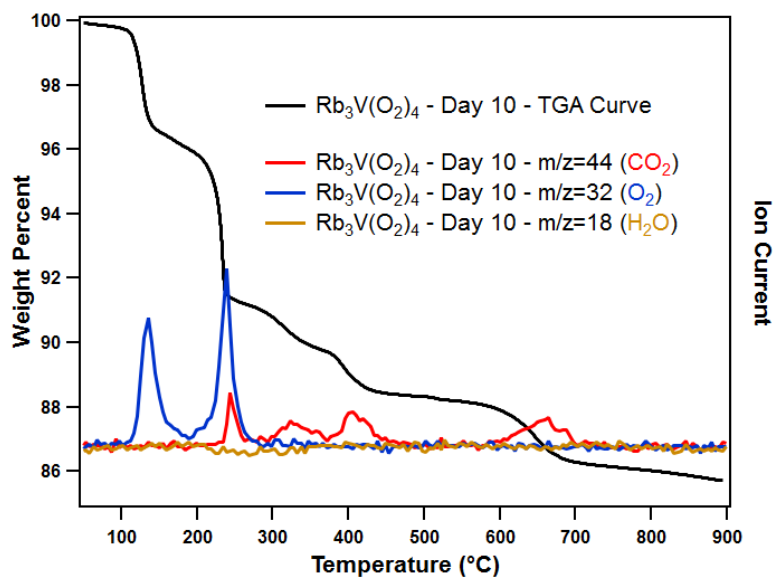


Figure S21. TGA curve and MS spectra for $\text{Rb}_3\text{V}(\text{O}_2)_4$ after being exposed to ambient conditions for 10 days. The CO_2 has a weight percent of 7.20 %; the O_2 is 5.30 %, and the water only takes 1.77 %.

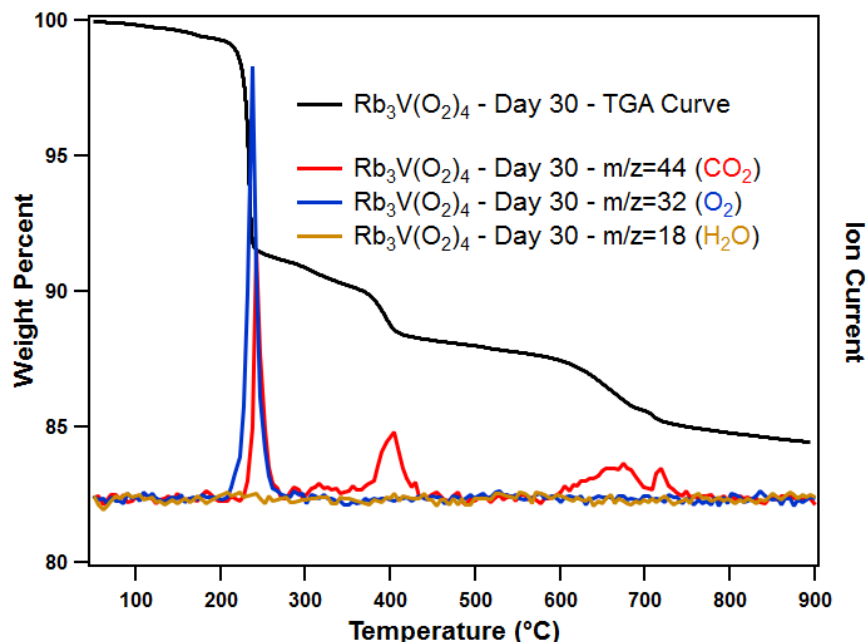


Figure S22. TGA-MS spectrum for $\text{Rb}_3\text{V}(\text{O}_2)_4$ after being exposed to ambient conditions for 30 days. The O_2 signals were concentrated within the temperature range of 200 – 300 °C, while the CO_2 peaks were found at 250 °C, 400 °C, and 675 °C. The CO_2 has a weight percent of 9.43 %; the O_2 is 5.30 %, and the water only takes 0.84 %.

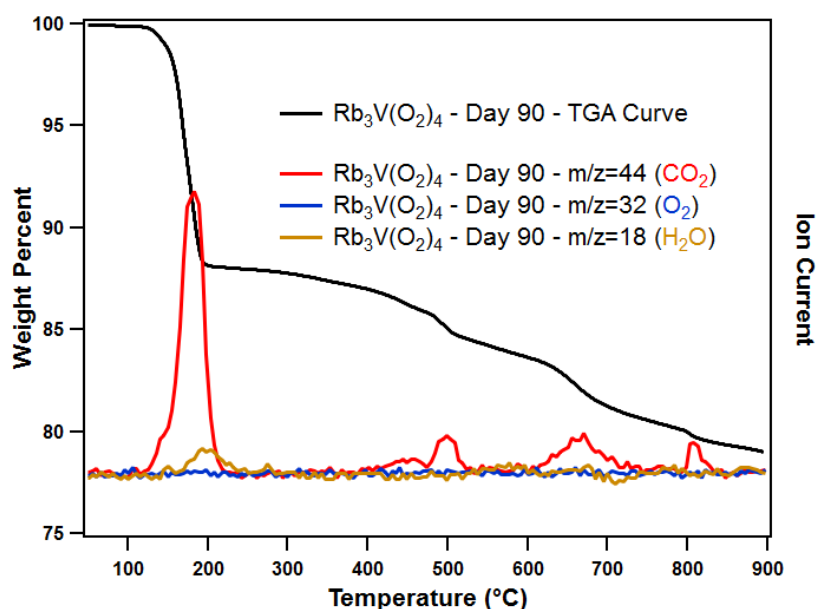


Figure S23. TGA-MS spectrum for $\text{Rb}_3\text{V}(\text{O}_2)_4$ being exposed to ambient conditions for 90 days. A strong CO_2 peak was found at 185 °C and O_2 content disappeared, which indicate more CO_2 absorbed by this product. The CO_2 has a weight percent of 17.46 % and the water takes 3.54 %.

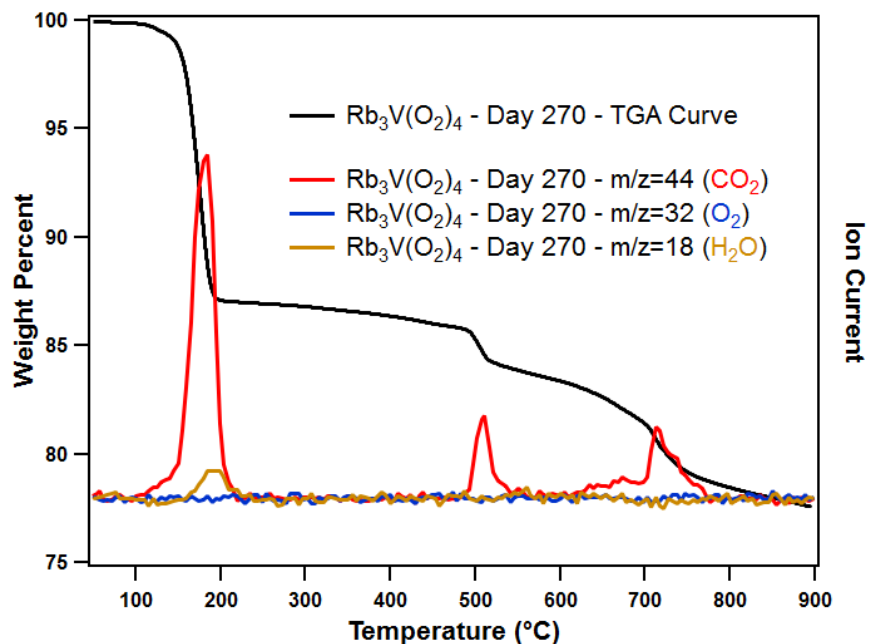


Figure S24. TGA-MS spectrum for $\text{Rb}_3\text{V}(\text{O}_2)_4$ after capturing carbon dioxide under ambient conditions for 270 days. The CO_2 has a weight percent of 18.35 % and the water takes 4.09 %.

Table S6. Results of TGA-MS Data of $\text{Cs}_3\text{V}(\text{O}_2)_4$ Carbon Capture Time Study Experiments under Ambient Conditions.

Species	CO_2 %	O_2 %	H_2O %	C%	C:V Ratio
Fresh	-	11.1	0.82	-	-
Day 3	3.03	8.70	0.63	0.82	0.40
Day 8	4.24	8.54	0.18	1.16	0.57
Day 18	4.13	8.33	0.23	1.12	0.55
Day 45	10.8	0.24	2.36	2.95	1.46
Day 150	12.8	-	2.67	3.48	1.76

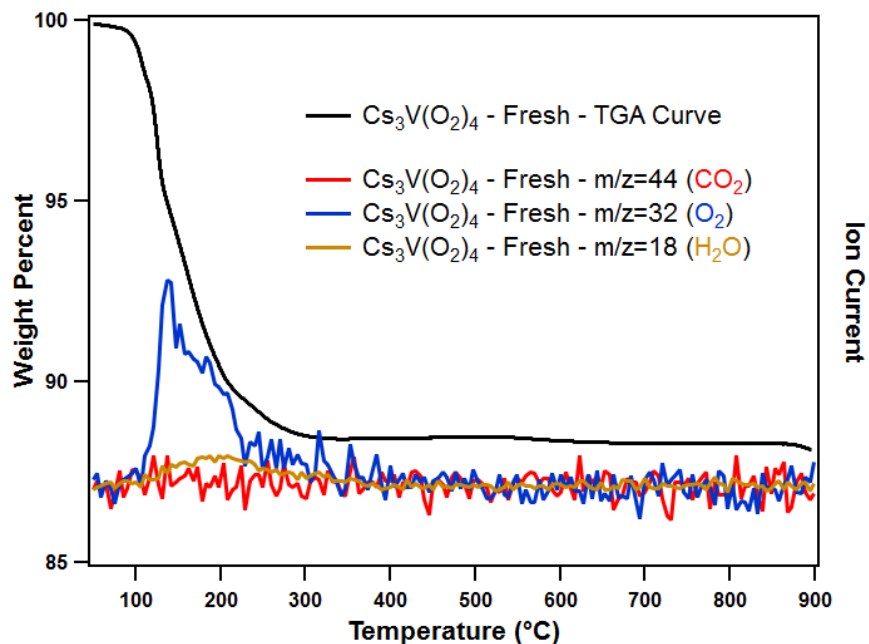


Figure S25. TGA curve and MS spectra for fresh synthesized $\text{Cs}_3\text{V}(\text{O}_2)_4$. The weight loss in the temperature range of 80 °C to 250 °C is assigned to four peroxide ligands bonded to the vanadium center (experimental: 11.28 wt %, theoretical: 11.08 wt %).

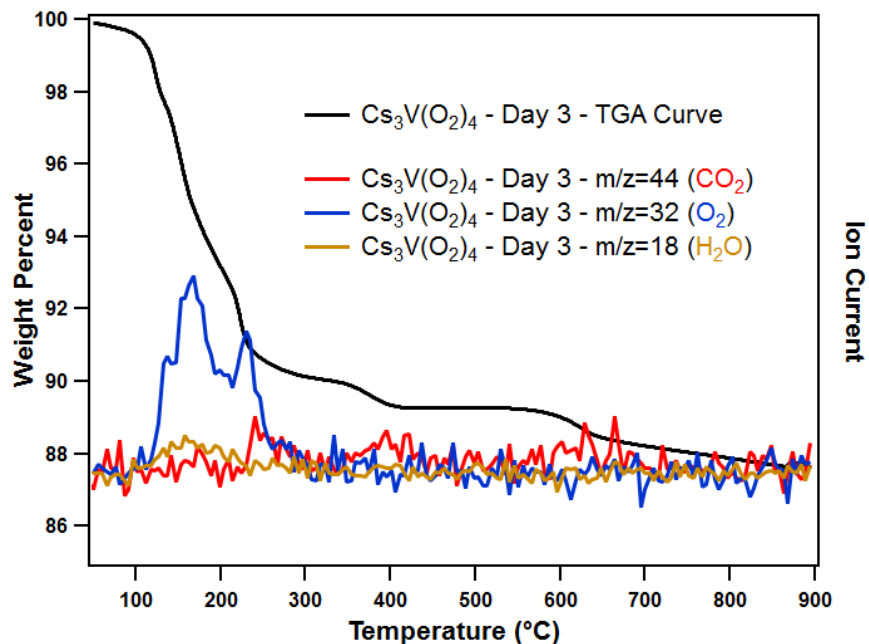


Figure S26. TGA curve and MS spectra for $\text{Rb}_3\text{V}(\text{O}_2)_4$ after being exposed to ambient conditions for 3 days. The TGA-MS shows a stepwise thermal decomposition process associated with (i) molecular oxygen from unreacted peroxide ligands bound to the vanadium metal center (100 – 195 °C), (ii) oxygen and carbon dioxide from peroxides and carbonates bonded to vanadium (195 – 300 °C), and (iii) carbon dioxide from carbonates bonded to alkali metals (300 – 900 °C). The CO_2 has a weight percent of 3.03 %; the O_2 is 8.70 %, and the water takes 0.63 %.

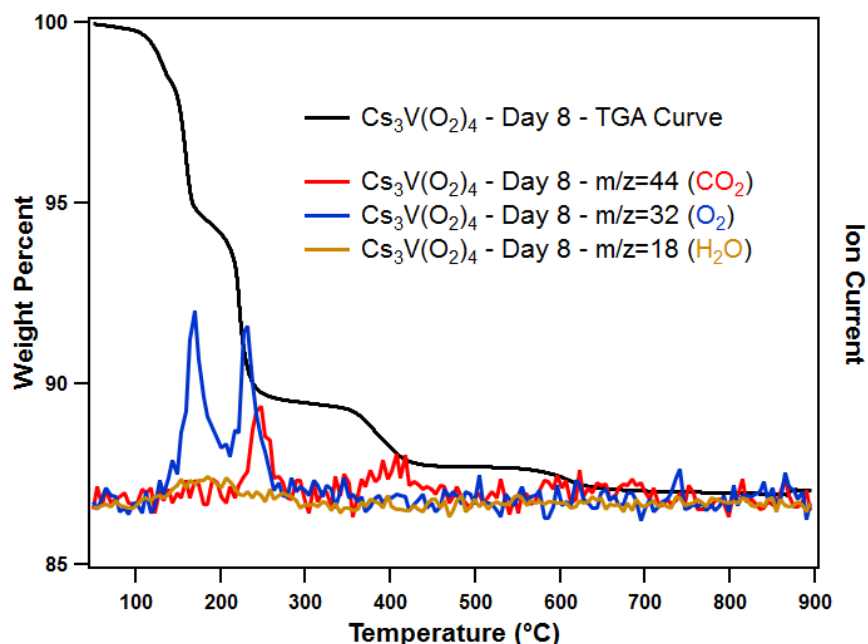


Figure S27. TGA curve and MS spectra for $\text{Cs}_3\text{V}(\text{O}_2)_4$ after being exposed to ambient conditions for 8 days.-The CO_2 has a weight percent of 4.24 %; the O_2 is 8.54 %, and the water only takes 0.18 %.

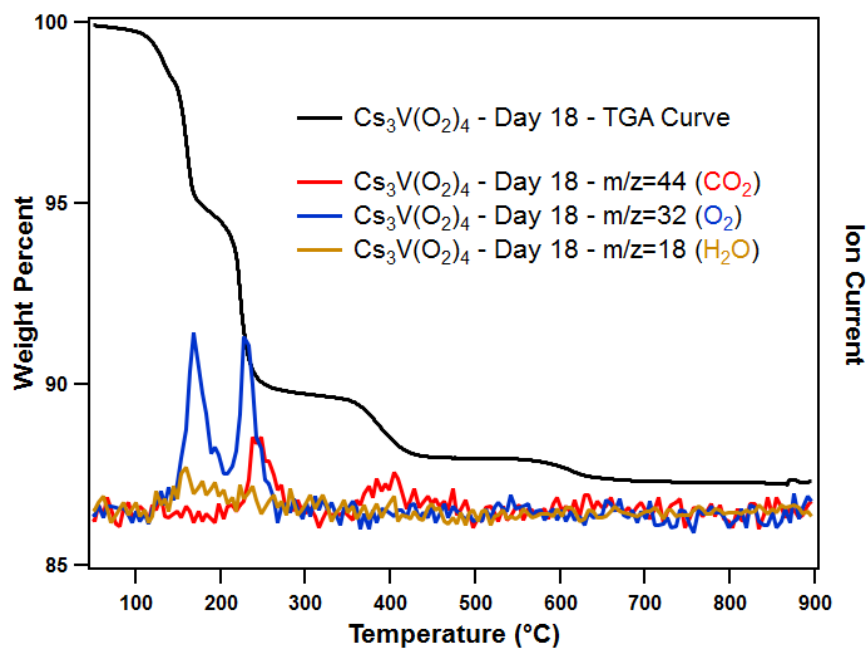


Figure S28. TGA-MS spectrum for $\text{Cs}_3\text{V}(\text{O}_2)_4$ after being exposed to ambient conditions for 18 days. The O_2 signals were concentrated within the temperature range of 150 – 300 $^{\circ}\text{C}$, while the CO_2 peaks were found at 250 $^{\circ}\text{C}$, 400 $^{\circ}\text{C}$, and 620 $^{\circ}\text{C}$. The CO_2 has a weight percent of 4.13 %; the O_2 is 8.33 %, and the water only takes 0.23 %.

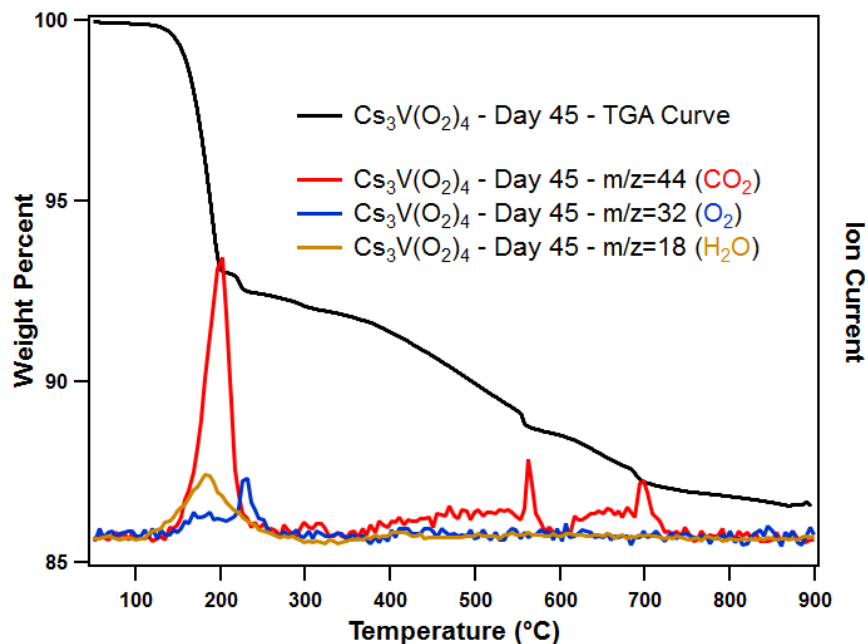


Figure S29. TGA-MS spectrum for $\text{Cs}_3\text{V}(\text{O}_2)_4$ being exposed to ambient conditions for 45 days. A strong CO_2 peak was found at 200 °C and O_2 content is almost disappeared, which indicate more CO_2 absorbed by this product. The CO_2 has a weight percent of 10.82 % and the water takes 2.36 %.

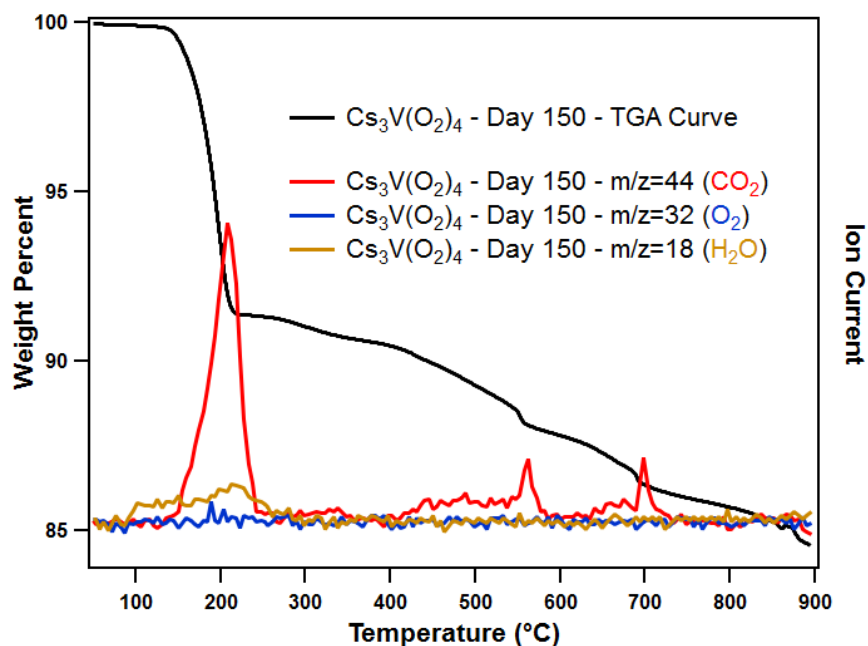


Figure S30. TGA-MS spectrum for $\text{Cs}_3\text{V}(\text{O}_2)_4$ after capturing carbon dioxide under ambient conditions for 150 days. The CO_2 has a weight percent of 12.77 % and the water takes 2.67 %.

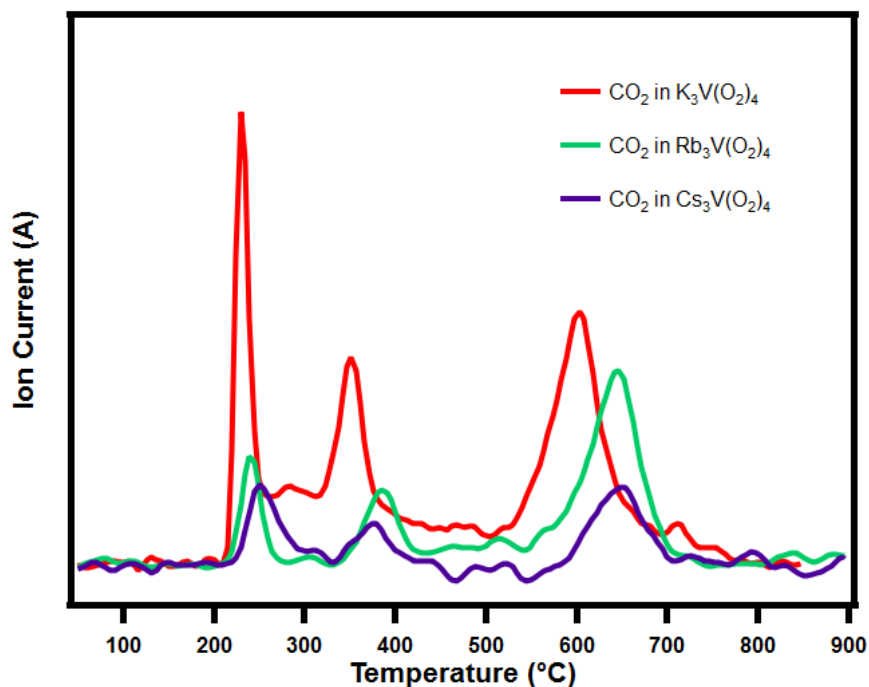


Figure S31. MS spectra for all three analogues after capturing carbon dioxide under ambient conditions for 10 days. The CO₂ signal was first detected at 220 °C comparing with the decomposition of peroxides.

CHN Analysis

Table S7. Tetraperoxovanadate CO₂ Capture Performance under ambient condition by TGA-MS

Material (Powder)	Carbon Weight Percent	Carbon Captured per Molecule	CO ₂ capture capacity (mmol/g)
K ₃ V(O ₂) ₄ (270 Days)	5.77	1.51	5.10
Rb ₃ V(O ₂) ₄ (270 Days)	5.00	1.91	4.39
Cs ₃ V(O ₂) ₄ (150 Days)	3.48	1.76	3.05

Table S8. Tetraperoxovanadate CO₂ Capture Performance under ambient condition by CHN

Material (Powder)	Carbon Weight Percent	Carbon Captured per Molecule	CO ₂ capture capacity (mmol/g)
K ₃ V(O ₂) ₄ (300 Days)	5.58	1.46	4.93
Rb ₃ V(O ₂) ₄ (300 Days)	5.02	1.92	4.41
Cs ₃ V(O ₂) ₄ (300 Days)	3.14	1.56	2.70

Table S9. Tetraperoxovanadate CO₂ Capture Performance Comparison

Material (Powder)	Carbon Captured per Molecule by TGA-MS	Carbon Captured per Molecule by CHN
K ₃ V(O ₂) ₄	1.51	1.46
Rb ₃ V(O ₂) ₄	1.91	1.92
Cs ₃ V(O ₂) ₄	1.61	1.56

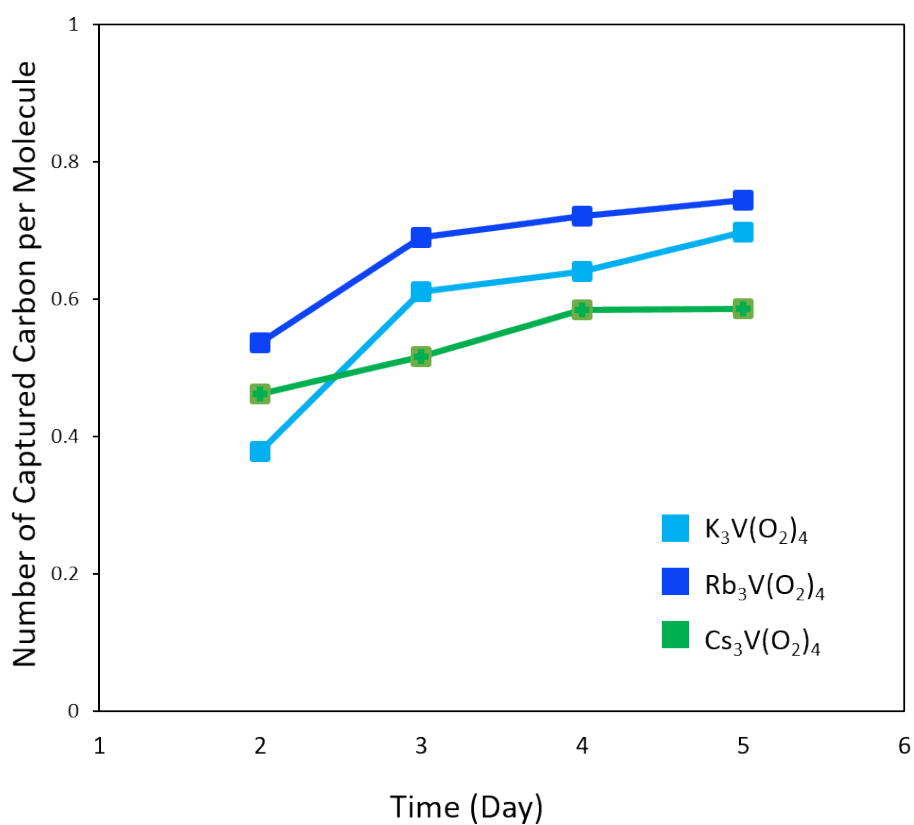


Figure S32. Carbon dioxide captured by per tetraperoxovanadate under ambient condition in the first five days.

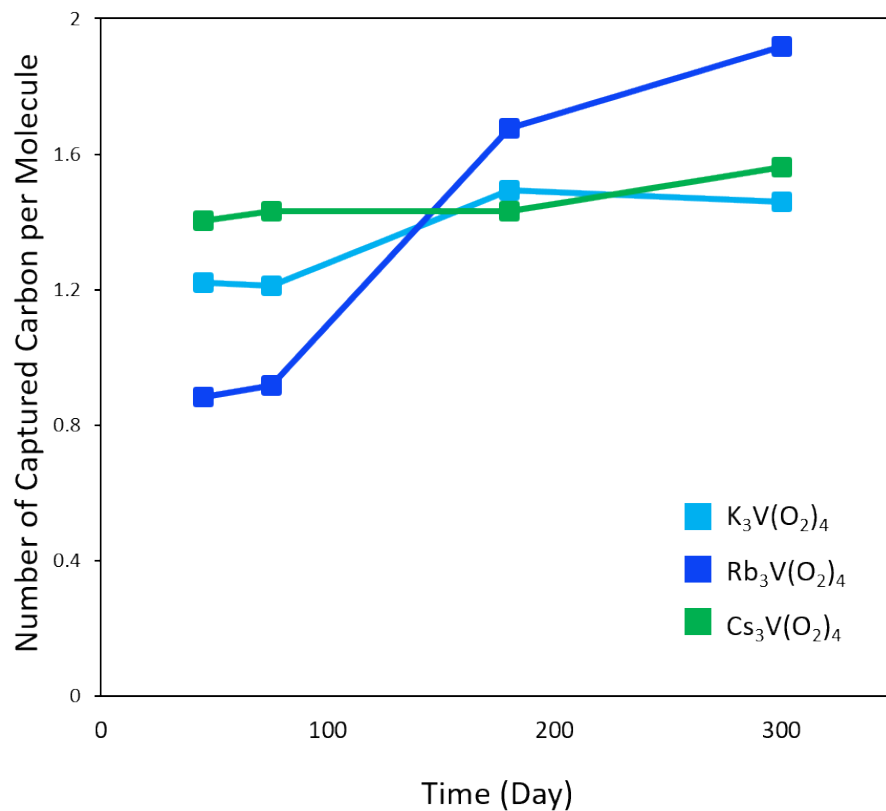


Figure S33. Carbon dioxide captured by per tetraperoxovanadate under ambient condition during the last 200 days of monitoring.

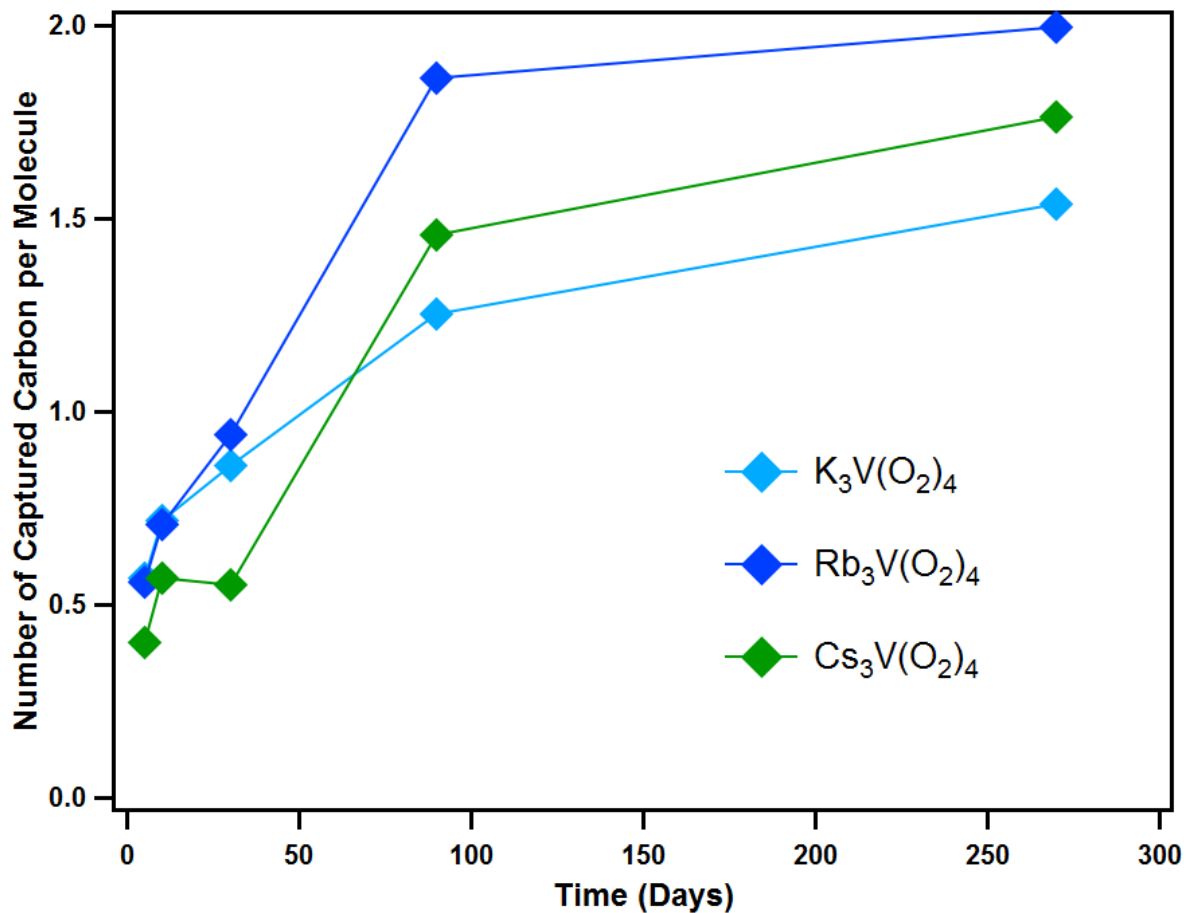


Figure S34. Carbon capture performance for decomposed $A_3V(O_2)_4$ analogues under ambient conditions calculated by combining TGA-MS results.

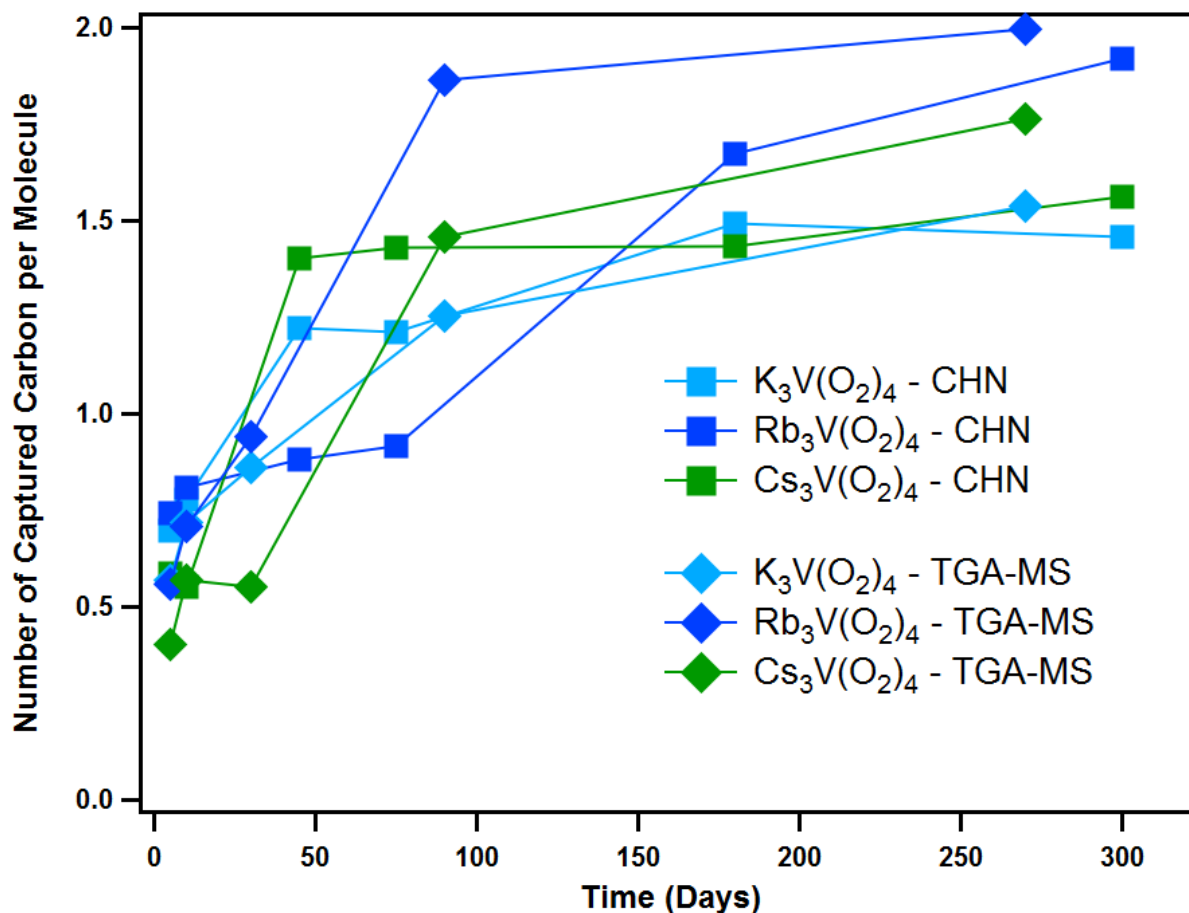


Figure S35. Stacked patterns of carbon capture performance for decomposed $A_3V(O_2)_4$ analogues under ambient conditions determined by CHN and TGA-MS methods.

$$\begin{aligned} \text{Carbon captured per mole} &= \frac{\text{moles of carbon}}{\text{moles of tetraperoxovanadate}} \\ &= \frac{\text{Carbon Weight\%} / \text{Molar Mass of Carbon}}{(1 - \text{Carbon Weight\%}) / \text{Molar Mass of the Tetraperoxide}} \end{aligned}$$

The calculation above is based on Equation S1.

Equation S1. Equation used to calculate the amount of carbon captured per molecule

Superoxide Characterization

NBT Tests

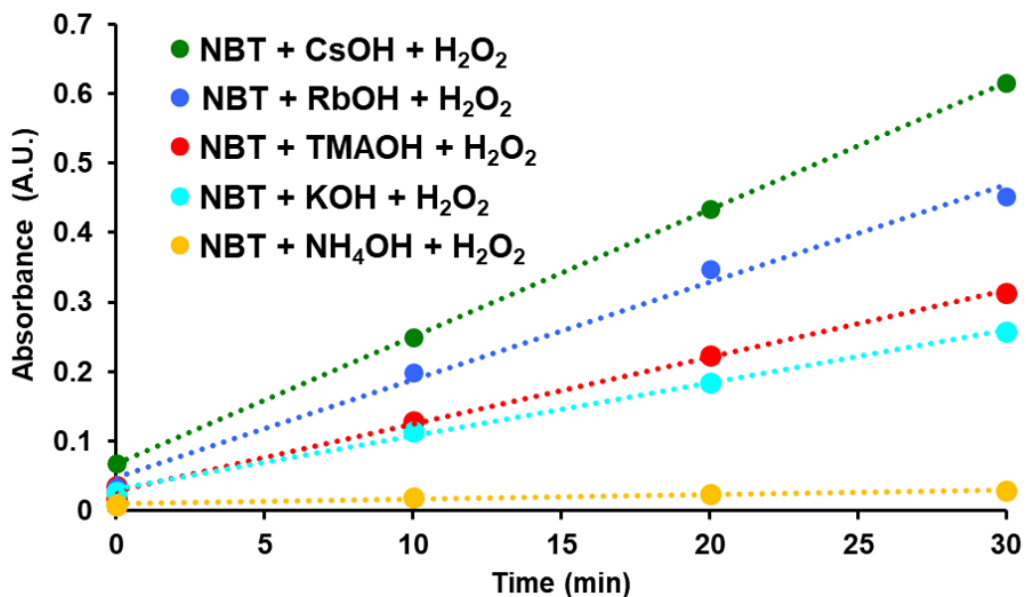


Figure S36. Absorbance over time of different hydroxides in water at 551 nm. Adding H₂O₂ to an aqueous solution of a hydroxide and NBT causes a colour change from yellow to purple. The colour intensity of the solution increases with time.

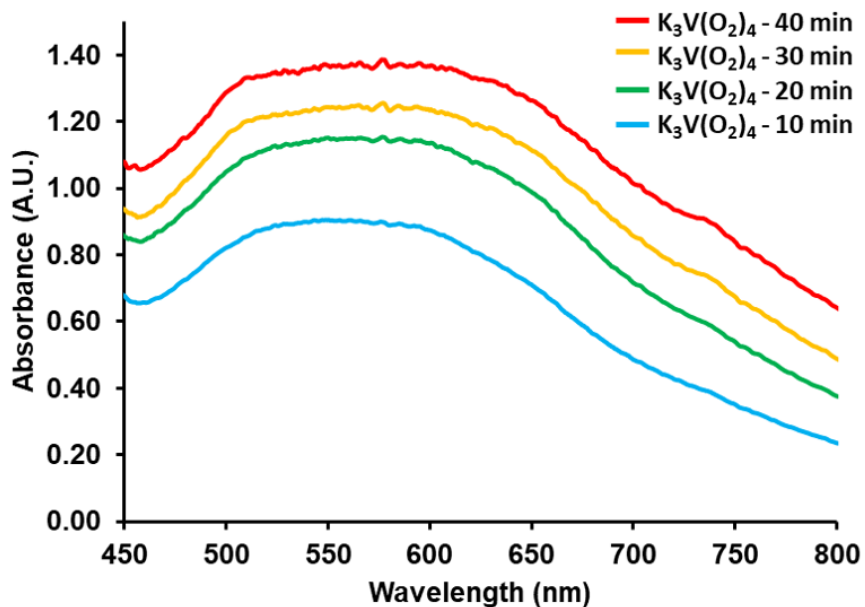


Figure S37. Full absorbance spectrum of K₃V(O₂)₄ at different time stamps. The reduction product of NBT (formazan) displays its maximum intensity at 551 nm.

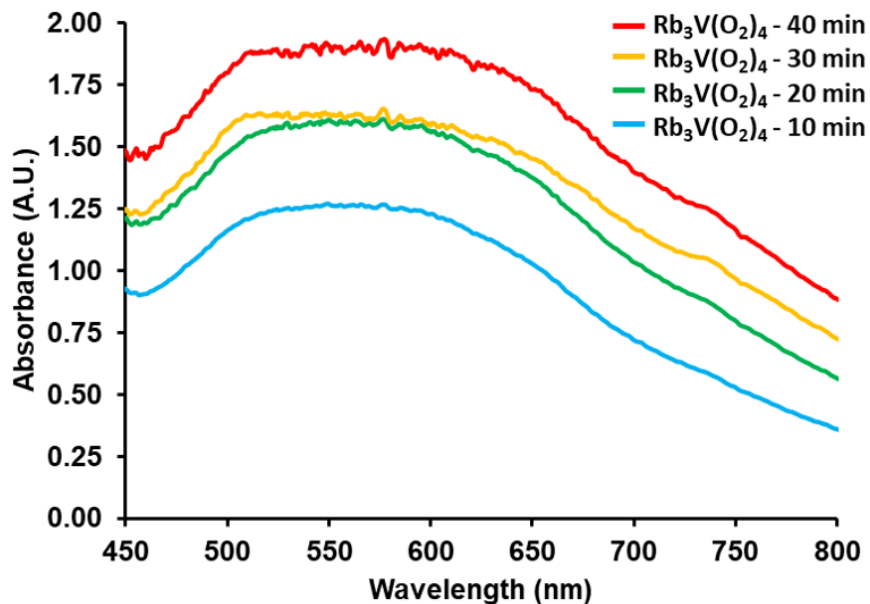


Figure S38. Absorbance of $\text{Rb}_3\text{V}(\text{O}_2)_4$ at different time stamps. The reduction product of NBT (formazan) displays its maximum intensity at 551 nm.

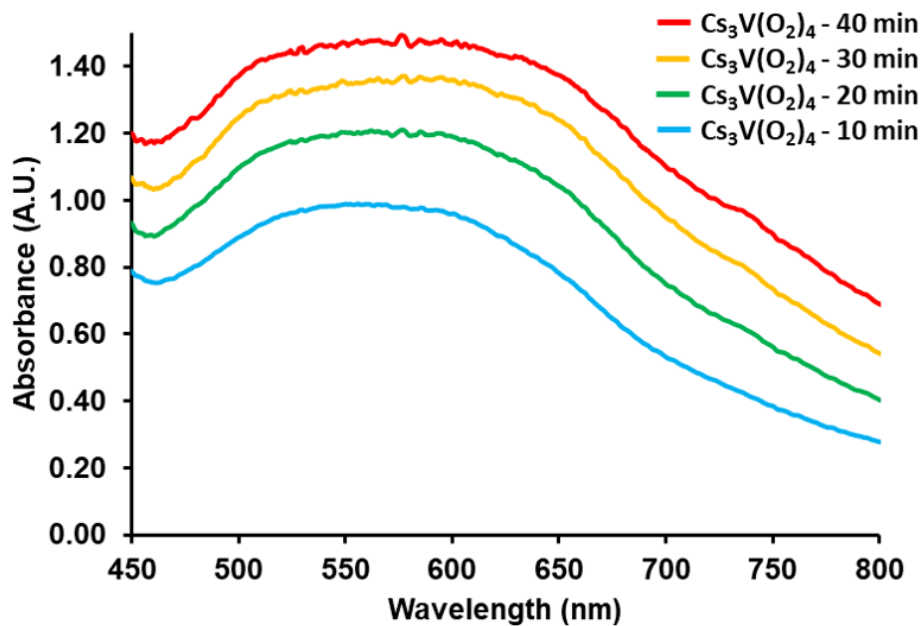


Figure S39. Absorbance of $\text{Cs}_3\text{V}(\text{O}_2)_4$ at different time stamps. The reduction product of NBT (formazan) displays its maximum intensity at 551 nm.

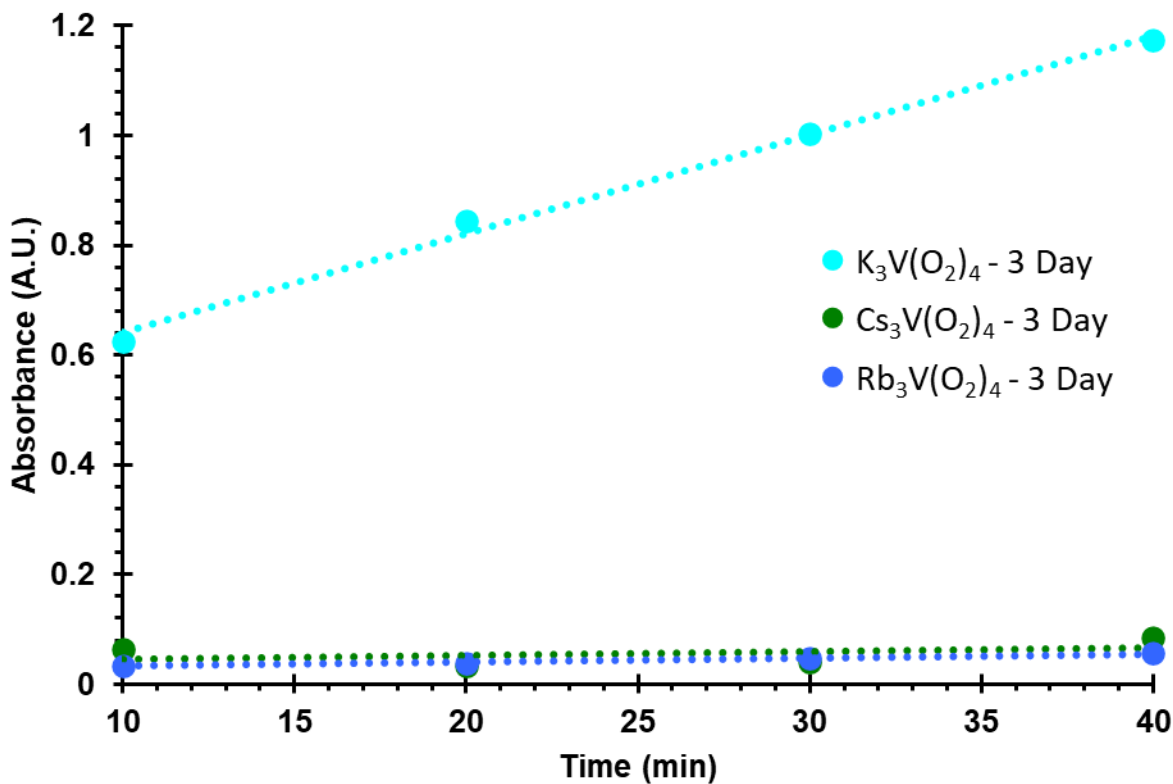


Figure S40. Absorbance rate (551 nm) of $A_3V(O_2)_4$ analogues after 3 days exposed to air. The Rb and Cs analogues decomposed rapidly and by the time the samples were reacted with NBT the solid had fully changed colour to yellow. $K_3V(O_2)_4$ retained the purple colour characteristic of the fresh materials and presented a similar behaviour to that of a fresh sample.

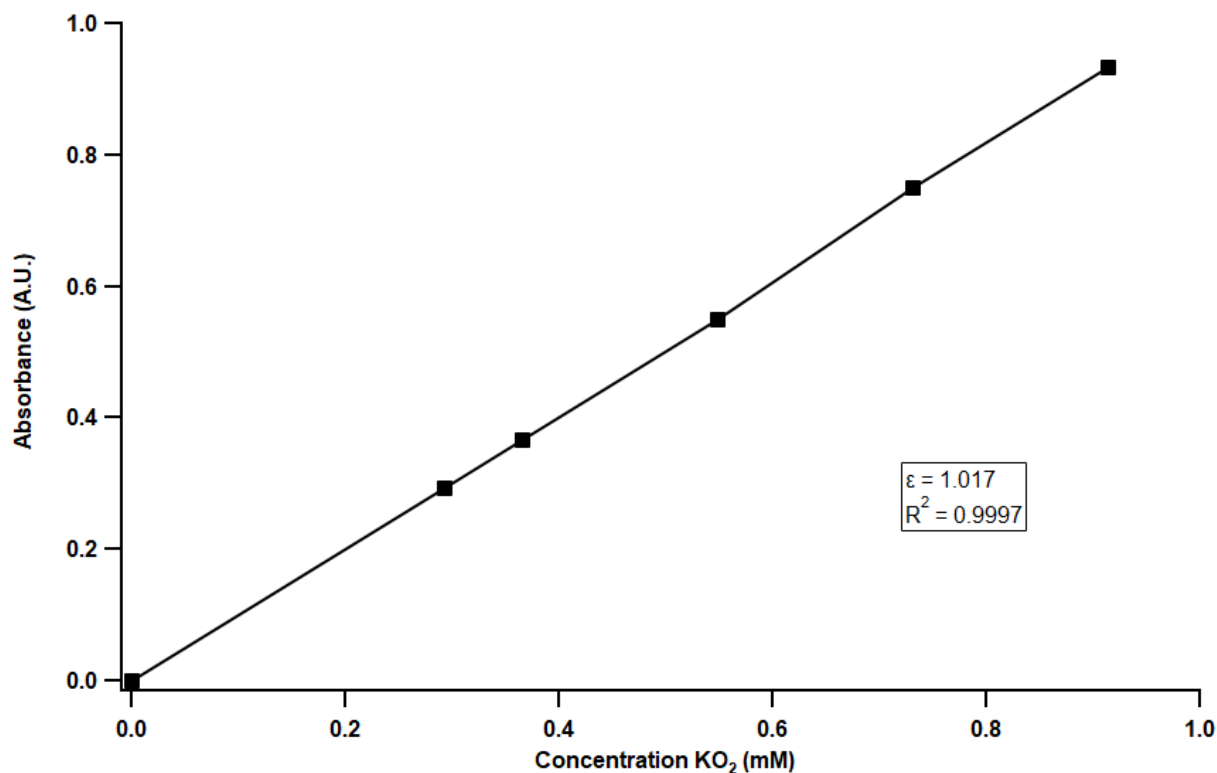


Figure S41. KO_2 calibration curve. Different dilutions of an aqueous KO_2 -NBT solution were prepared and measured. The maximum absorbance at 551 nm was plotted vs. the concentration of KO_2 to allow for quantification of KO_2 in the tetraperoxovanadate materials.

Table S10. Comparison between different fits for the trend line of concentration of superoxide vs. time for $\text{A}_3\text{V}(\text{O}_2)_4$ from the NBT tests

Compound	R^2 Linear Fit	R^2 Power Fit
$\text{K}_3\text{V}(\text{O}_2)_4$	0.95239	0.98863
$\text{Rb}_3\text{V}(\text{O}_2)_4$	0.91504	0.93972
$\text{Cs}_3\text{V}(\text{O}_2)_4$	0.97961	0.99999

EPR Characterization

Table S11. EPR data summary (100K)

Phase	g_{parallel}	$g_{\text{perpendicular}}$	Mole% superoxide ¹
$\text{K}_3\text{V}(\text{O}_2)_4$	2.148 2.128	2.013	4.9
$\text{Rb}_3\text{V}(\text{O}_2)_4$	2.157 2.136	2.014	5.1
$\text{Cs}_3\text{V}(\text{O}_2)_4$	2.113	2.016	4.2
KO_2/DMSO	2.113	2.014	N/A

¹assuming peroxide replacement with superoxide; i.e. $A_{3-x}\text{V}(\text{O}^{2-}_2)_{4-x}(\text{O}^{1-}_2)_x$

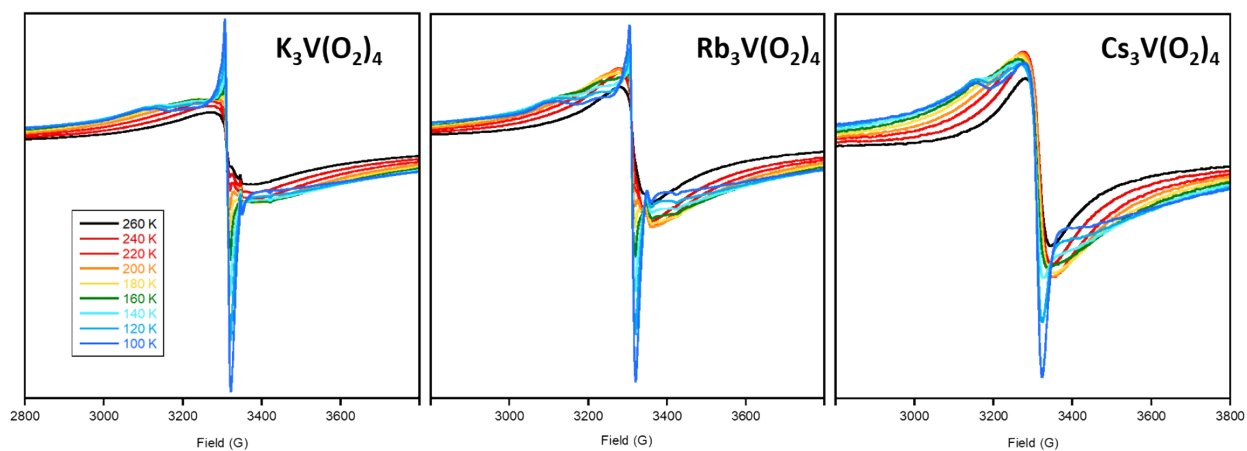


Figure S42. Variable temperature EPR spectra collected between 100 K and 260 K.

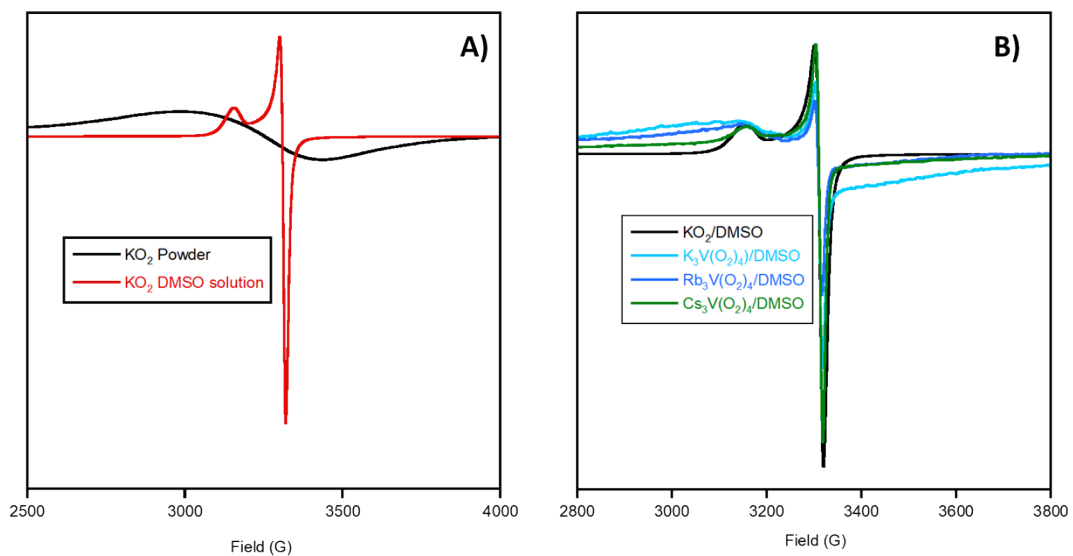
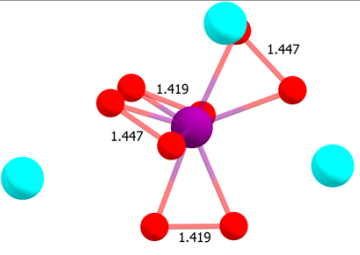
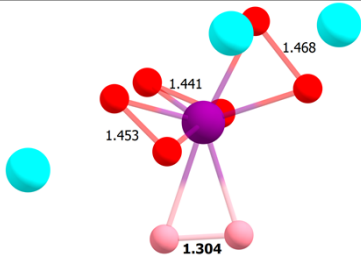
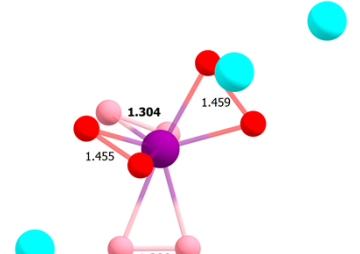


Figure S43. A) Potassium superoxide EPR spectra at 100 K. KO_2 powder as received (black), KO_2 dissolved in DMSO (red). The broad, featureless spectrum of the powder is due to magnetic interactions between neighboring paramagnetic sites. When dissolved in a solvent, the spin-spin distance increases allowing the spectrum to reflect an isolated radical. **B)** EPR spectra in DMSO solutions at 100 K. Compounds were vortexed in DMSO, then spun down in a centrifuge and the supernatant collected.

Exploring superoxide through computation.

Table S12. Calculated energies of spin states for vanadium peroxo-superoxocomplexes. In the DFT-optimized structures, peroxide ligands are depicted in red and superoxide ligands are shown in salmon. Select bond lengths are provided in Å. (D) Relative room-temperature Gibbs free energies (with raw electronic energies in parentheses) of the considered spin states for $K_3V(O_2)_4$, $Rb_3V(O_2)_4$, and $Cs_3V(O_2)_4$ in kcal/mol. Peroxo/superoxo designations were based on the calculated O-O bond lengths and Mulliken spin densities. The triplet state corresponds to having one unpaired electron on the vanadium, forming V^{4+} , and another on one of the ligands, forming O_2^- superoxide. Given the small energy difference between the singlet (4 peroxide) and triplet state (3 peroxide and 1 superoxide), some amount of superoxide is expected to be present in all $A_3V(O_2)_4$ samples at room temperature; the quintet state (2 peroxide and 2 superoxide) is predicted to be energetically inaccessible in all cases.

$A_3V(O_2)_4$	S=0, singlet	S=1, triplet	S=2, quintet
K	0.0 (0.0), 4 peroxo	0.9 (1.6), 3 peroxo, 1 superoxo	45.0 (47.1); 2 peroxo, 2 superoxo
Rb	0.0 (0.0), 4 peroxo	1.6 (3.0), 3 peroxo, 1 superoxo	39.0.0 (42.1); 2 peroxo, 2 superoxo
Cs	0.0 (0.0), 4 peroxo	2.7 (4.3), 3 peroxo, 1 superoxo	37.2 (40.0); 2 peroxo, 2 superoxo
<i>Illustrations of singlet, triplet and quintet</i>			
			

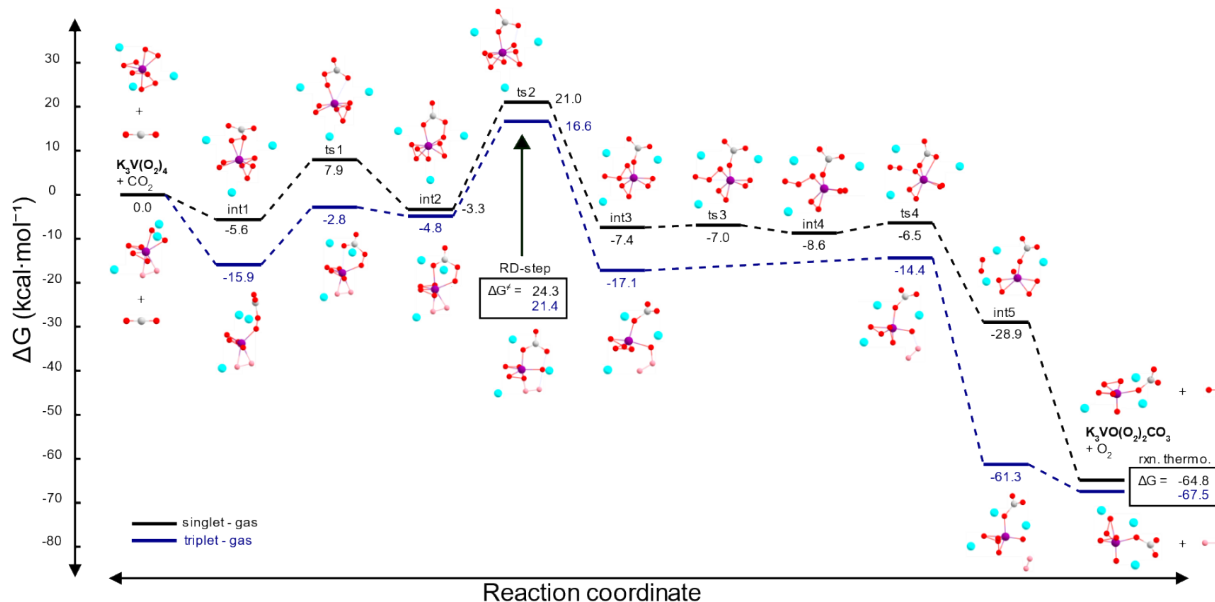


Figure S44. DFT reaction mechanism for $\text{K}_3\text{V}(\text{O}_2)_4 + \text{CO}_2 \rightarrow \text{K}_3\text{VO}(\text{O}_2)_2\text{CO}_3 + \text{O}_2$. ts=transition state, int=intermediate. The relative energies on the singlet potential energy surface are shown in black with the corresponding structures above (identical to Figure S11). The steps on the triplet surface are in blue with the structures below, which include some superoxide oxygen atoms depicted in salmon red. The triplet mechanism involves the superoxide ligand starting in ts2 in which an oxygen atom is transferred to it, generating O_3^- . In the subsequent step, ts4, one of the O-O bonds in O_3^- is cleaved to produce $^3\text{O}_2$ and singlet $\text{K}_3\text{VO}(\text{O}_2)_2\text{CO}_3$, thereby removing superoxide from the complex. In terms of the impact on carbon capture reactivity, superoxide ligands slightly lower the barrier of the rate-determining step (~ 3 kcal/mol), ts2, and increase the thermodynamic driving force by approximately the same amount. A direct reaction between CO_2 and the superoxide ligand was explored but seems to be incapable of proceeding beyond int1. Note that the final product in both spin cases consists of a singlet $\text{K}_3\text{VO}(\text{O}_2)_2\text{CO}_3$ and triplet O_2 .

Carbon Capture technologies overview

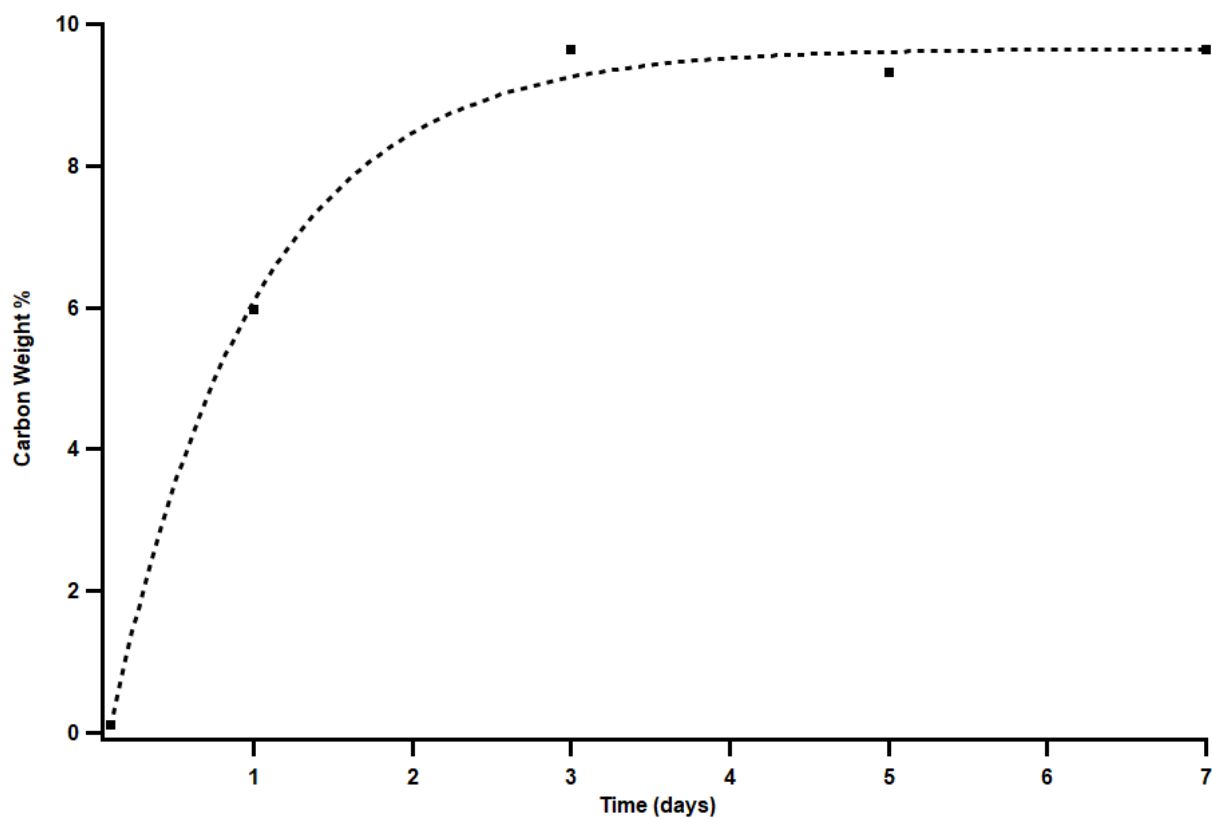


Figure S45. Carbon capture of Na_2O_2 exposed to atmospheric conditions over time. The fresh material reaches its maximum carbon content of 9.6 % after 3 days, at which point remains constant.

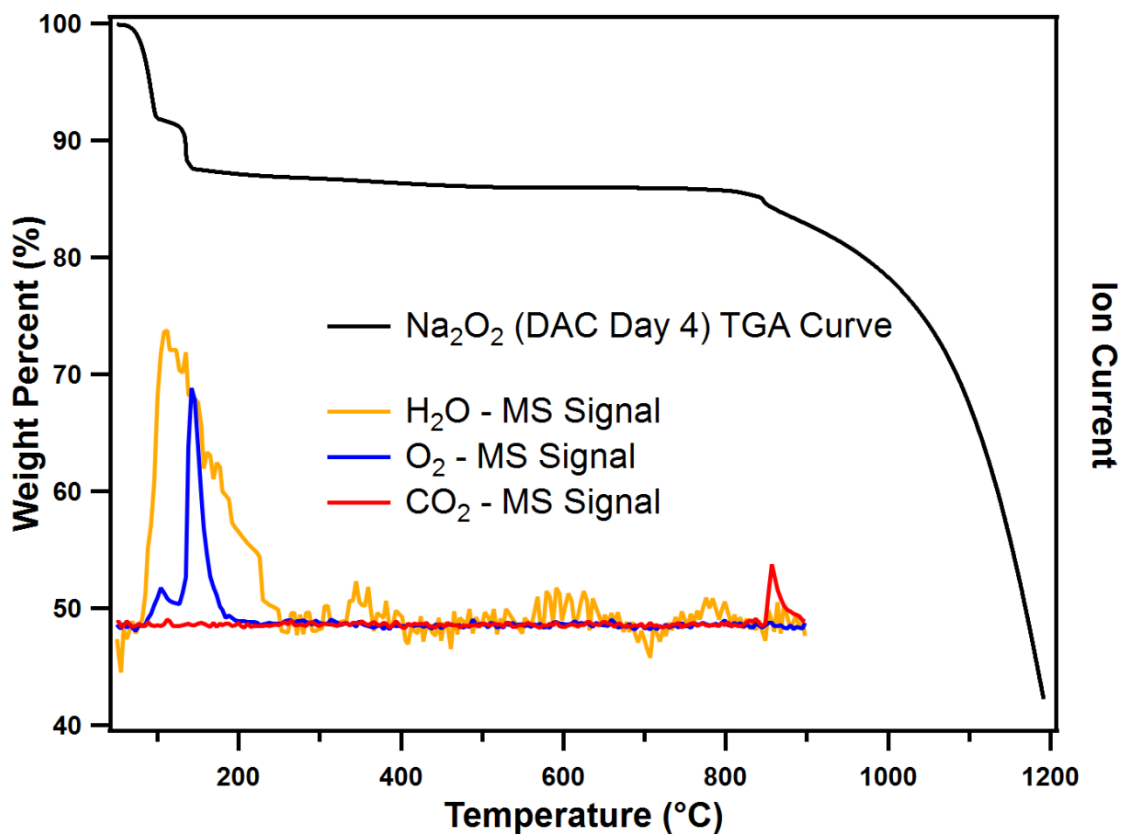


Figure S46. TGA-MS spectrum of Na₂O₂ exposed to air for 4 days. The initial weight loss below 100 °C is assigned to water captured. Oxygen from unreacted material is released right after. There are no MS signals from CO₂ below 800 °C. Beyond this point the MS signals become unreliable and thus are cut. The final weight loss starting around 900 °C is due to the high temperature release of CO₂ captured.

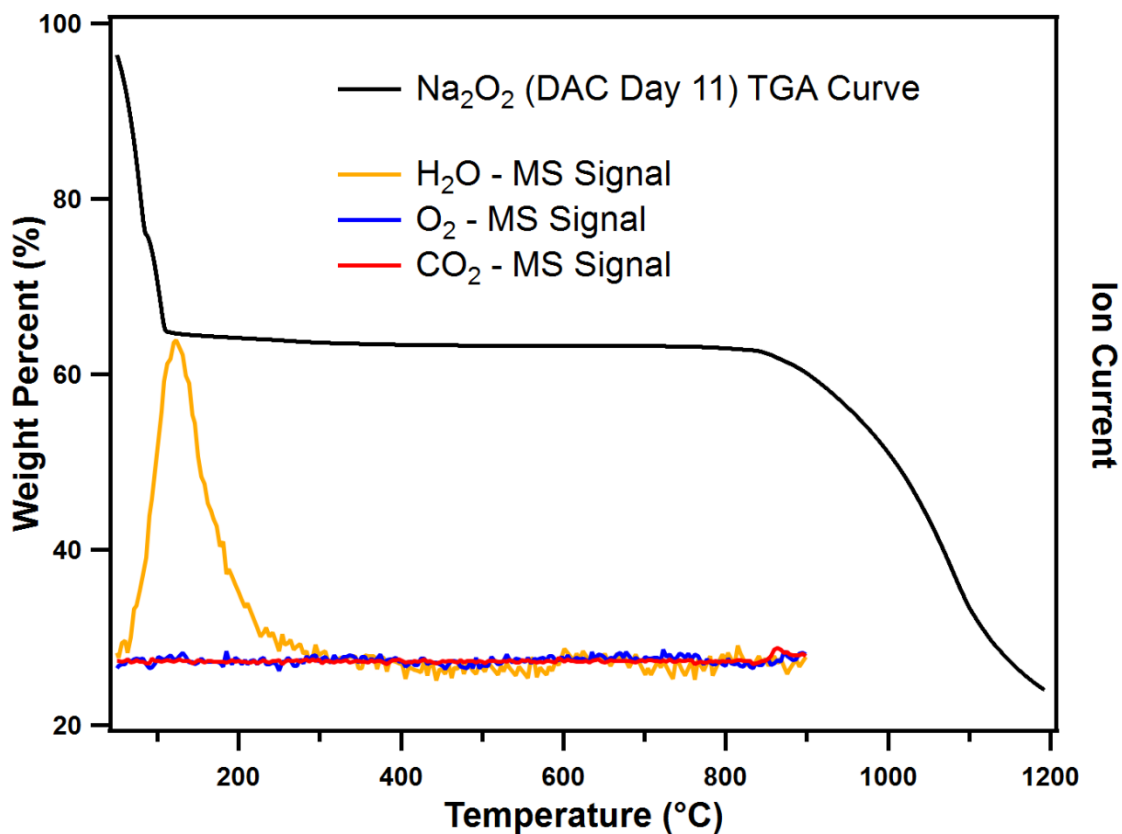


Figure S47. TGA-MS spectrum of Na_2O_2 exposed to air for 11 days, when there was an increase in the ambient humidity. The initial water peak that previously accounted for less than 5 % weight loss now accounts for over 30 % of the material. The lack of an oxygen signal indicates that all of the Na_2O_2 has reacted. As above, the CO_2 release starts around 900 $^{\circ}\text{C}$.

Table S13. A comparison between select technologies for carbon capture.

Absorption / adsorption type	Carbon Capture Material	Modification scheme	Temp. (°C)	Carbon capture conditions	Capacity (mmol g ⁻¹)	Ref.
Liquid-based CO ₂ capture system	Liquid amine-based solvents	Blended amine solvents	40	100% CO ₂ , until equilibrium	1.01	17
	Ionic liquid-based solvents	Amine- or amino-acid-functionalized ILs	40	100% CO ₂ , 5 bar, for 4 h	1.60	
Low-temperature solid CO ₂ adsorbents	Solid amine-based adsorbents	Silica as supporting materials	85	95% CO ₂ , 5% N ₂ , for 3 h	3.28	
		MOFs	40	15% CO ₂ , 85% He, for 30 min	4.06	
		Clays	60	15% CO ₂ , 3% O ₂ , 10% H ₂ O, and 2% Ar in N ₂ balance	4.05	
		Polymers	25	Moist CO ₂ /N ₂ gas	2.92	
	Carbon-based adsorbents	Tuning the textural properties	25	100% CO ₂	4.80	
		Surface chemical modification	25	10% CO ₂ , 90% Ar, for 60 min	4.13	
	Zeolite-based adsorbents	Amines impregnation	30	100% CO ₂ , for 1 h	0.45	
		Hybrid preparation materials	25	100% CO ₂	1.62	
	MOF-based adsorbents	Functional component integration	25	15% CO ₂	1.63	
	Alkali carbonates-based adsorbents	—	60	10% CO ₂ , 10% H ₂ O, 80% N ₂	3.1	
Intermediate-temperature solid CO ₂ adsorbents	LDH-based adsorbents	Chemical composition tuning	200	100% CO ₂ , for 2 h	1.25	
		LDH-based composite	200	100% CO ₂ , for 2 h	0.47	
		Doping with alkali metals	240	100% CO ₂ , for 5 h	9.27	

	MgO-based adsorbents	Mesoporous structure fabrication	300	100% CO ₂ , for 4 h	1.22	
		Molten salts modification	300	100% CO ₂ , for 4 h	10.2	
High-temperature solid CO ₂ sorbents	CaO-based sorbents	Preparation of CaO nanoparticles	700	100% CO ₂ , for 30 min	17.18	
	Alkali silicate-based sorbents	Molten salts modification	650	100% CO ₂ , for 2 h	8.25	
	Alkali titanate-based sorbents	Binary alkali-metal titanate	700	20–100% CO ₂ , for 10 min	0.43	
Direct Air Carbon Capture	Solid amine-based (PEI) adsorbents	Com silica	25	atmospheric CO ₂ ¹	2.36	18
		Fumed silica	25	atmospheric CO ₂ ¹	2.44	
		Mesocellular silica	25	atmospheric CO ₂ ¹	1.74	
		γ-Alumina	25	atmospheric CO ₂ ¹	1.74	
		SBA-15 (75 wt% amine loading)	25	atmospheric CO ₂ ¹	1.90	
		MIL-101(Cr) (50 wt% amine loading)	25	atmospheric CO ₂ ¹	1.81	
Direct Air Carbon Capture (Peroxide)	Tetraperoxo-metalates	K ₃ V(O ₂) ₄	25	atmospheric CO ₂ ¹	4.93	This Work
		Rb ₃ V(O ₂) ₄	25	atmospheric CO ₂ ¹	4.41	
		Cs ₃ V(O ₂) ₄	25	atmospheric CO ₂ ¹	2.70	

¹approximately 400 ppm

References

1. P. Hohenberg and W. Kohn, Inhomogeneous Electron Gas. *Physical Review*, 136, B864. *Journal*, 1964.
2. W. Kohn and L. J. Sham, Self-consistent equations including exchange and correlation effects, *Phys. Rev.*, 1965, **140**, A1133.
3. S. Clark, M. Segall, C. Pickard, P. Hasnip, M. Probert, K. Refson and M. C. Payne, First Principles Methods Using CASTEP, *Z. Kristallogr. Cryst. Mater.*, 2005, **220**, 567.
4. J. P. Perdew, K. Burke and M. Ernzerhof, Generalized Gradient Approximation Made Simple, *Phys. Rev. Lett.*, 1996, **77**, 3865-3868.
5. B. G. Pfrommer, M. Côté, S. G. Louie and M. L. Cohen, Relaxation of Crystals with the Quasi-Newton Method, *J. Comput. Phys.*, 1997, **131**, 233-240.
6. H. J. Monkhorst and J. D. Pack, Special points for Brillouin-zone integrations, *Phys. Rev. B*, 1976, **13**, 5188-5192.
7. K. Refson, P. R. Tulip and S. J. Clark, Variational density-functional perturbation theory for dielectrics and lattice dynamics, *Phys. Rev. B*, 2006, **73**, 155114.
8. A. Jain, S. P. Ong, G. Hautier, W. Chen, W. D. Richards, S. Dacek, S. Cholia, D. Gunter, D. Skinner, G. Ceder and K. A. Persson, Commentary: The Materials Project: A materials genome approach to accelerating materials innovation, *APL Mater.*, 2013, **1**.
9. Jmol: an open-source Java viewer for chemical structures in 3D. <http://www.jmol.org/>.
10. G. W. T. M. J. Frisch, H. B. Schlegel, G. E. Scuseria, M. A. Robb, J. R. Cheeseman, G. Scalmani, V. Barone, G. A. Petersson, H. Nakatsuji, X. Li, M. Caricato, A. V. Marenich, J. Bloino, B. G. Janesko, R. Gomperts, B. Mennucci, H. P. Hratchian, J. V. Ortiz, A. F. Izmaylov, J. L. Sonnenberg, D. Williams-Young, F. Ding, F. Lipparini, F. Egidi, J. Goings, B. Peng, A. Petrone, T. Henderson, D. Ranasinghe, V. G. Zakrzewski, J. Gao, N. Rega, G. Zheng, W. Liang, M. Hada, M. Ehara, K. Toyota, R. Fukuda, J. Hasegawa, M. Ishida, T. Nakajima, Y. Honda, O. Kitao, H. Nakai, T. Vreven, K. Throssell, J. A. Montgomery, Jr., J. E. Peralta, F. Ogliaro, M. J. Bearpark, J. J. Heyd, E. N. Brothers, K. N. Kudin, V. N. Staroverov, T. A. Keith, R. Kobayashi, J. Normand, K. Raghavachari, A. P. Rendell, J. C. Burant, S. S. Iyengar, J. Tomasi, M. Cossi, J. M. Millam, M. Klene, C. Adamo, R. Cammi, J. W. Ochterski, R. L. Martin, K. Morokuma, O. Farkas, J. B. Foresman, and D. J. Fox, Gaussian 16, Revision A. 03, Gaussian, Inc., Wallingford CT, 2016, **3**.
11. T. Yanai, D. P. Tew and N. C. Handy, A new hybrid exchange–correlation functional using the Coulomb-attenuating method (CAM-B3LYP), *Chem. Phys. Lett.*, 2004, **393**, 51-57.
12. W. R. Wadt and P. J. Hay, Ab initio effective core potentials for molecular calculations. Potentials for main group elements Na to Bi, *Chem. Phys.*, 1985, **82**, 284-298.

13. I. Bytheway and M. W. Wong, The prediction of vibrational frequencies of inorganic molecules using density functional theory, *Chem. Phys. Lett.*, 1998, **282**, 219-226.
14. B. H. Solis, Y. Cui, X. Weng, J. Seifert, S. Schauer mann, J. Sauer, S. Shaikhutdinov and H.-J. Freund, Initial stages of CO₂ adsorption on CaO: a combined experimental and computational study, *PCCP*, 2017, **19**, 4231-4242.
15. R. Stomberg, The crystal structure of potassium carbonatooxidiperoxovanadate (V), K₃[VO(O₂)₂(CO₃)], *Acta Chem. Scand. A*, 1985, **39**, 725-731.
16. D. Wang, J. Zou, H. Cai, Y. Huang, F. Li and Q. Cheng, Effective degradation of Orange G and Rhodamine B by alkali-activated hydrogen peroxide: roles of HO₂⁻ and O₂^{·-}, *Environmental Science and Pollution Research*, 2019, **26**, 1445-1454.
17. W. Gao, S. Liang, R. Wang, Q. Jiang, Y. Zhang, Q. Zheng, B. Xie, C. Y. Toe, X. Zhu, J. Wang, L. Huang, Y. Gao, Z. Wang, C. Jo, Q. Wang, L. Wang, Y. Liu, B. Louis, J. Scott, A.-C. Roger, R. Amal, H. He and S.-E. Park, Industrial carbon dioxide capture and utilization: state of the art and future challenges, *Chem. Soc. Rev.*, 2020, **49**, 8584-8686.
18. D. Panda, V. Kulkarni, S. K. Singh and Engineering, Evaluation of amine-based solid adsorbents for direct air capture: a critical review, *React. Chem. Eng.*, 2023, **8**, 10-40.